Microstructure Analysis of Al-7 wt% Si Alloy Solidified on Earth Compared to Similar Experiments in Microgravity

András Roósz, Arnold Rónaföldi, Yuze Li, Nathalie Mangelinck-Noël, Gerhard Zimmermann, Henri Nguyen-Thi, Mária Svéda, Zsolt Veres

crystals

MDPI

Article

Microstructure Analysis of Al-7 wt% Si Alloy Solidified on Earth Compared to Similar Experiments in Microgravity

András Roósz [1,2,*], Arnold Rónaföldi [1,2], Yuze Li [3], Nathalie Mangelinck-Noël [4], Gerhard Zimmermann [5], Henri Nguyen-Thi [4], Mária Svéda [2] and Zsolt Veres [1]

1 Institute of Physical Metallurgy, Metal Forming, and Nanotechnology (U.M.), University of Miskolc, H-3515 Miskolc, Hungary
2 MTA-ME Materials Science Research Group, ELKH, H-3515 Miskolc, Hungary
3 School of Physical Science and Technology, Northwestern Polytechnical University, Xi'an 710100, China
4 Aix Marseille University, Université de Toulon, CNRS, IM2NP, 13013 Marseille, France
5 ACCESS e.V., Intzestrasse 5, D-52072 Aachen, Germany
* Correspondence: femroosz@uni-miskolc.hu

Abstract: During ground-based solidification, buoyancy flow can develop by the density difference in the hypoeutectic type of the alloys, such as Al-7 wt% Si alloy. Buoyancy flow can affect the thermal field, solute distribution in the melt, and the position and amount of the new grains. As solidification is a very complex process, it is not very easy to separate the different effects. Under microgravity conditions, natural convection does not exist or is strongly damped due to the absence of the buoyancy force. Therefore, experiments in microgravity conditions provide unique benchmark data for pure diffusive solidification conditions. Compared to the results of the ground-based and microgravity experiments, it is possible to get information on the effect of gravity (buoyancy force). In the framework of the CETSOL project, four microgravity solidification experiments were performed on grain refined (GF) and non-grain refined Al-7 wt% Si alloy onboard the International Space Station in the Materials Science Laboratory. These experiments aimed to study the effect of the solidification parameters (solid/liquid front velocity v_{SL}, temperature gradient G_{SL}) on the grain structure and dendritic microstructures. The microgravity environment eliminates the melt flow, which develops on Earth due to gravity. Four ground-based (GB) experiments were performed under Earth-like conditions with the same (similar) solidification parameters in a vertical Bridgman-type furnace having four heating zones. The detailed analysis of the grain structure, amount of eutectic, and secondary dendrite arm spacing (SDAS) for different process conditions is reported and compared with the results of the microgravity experiments. GB experiments showed that the microstructure was columnar in the samples that do not contain GF material or in case the solid/liquid (v_{SL} front velocity was slow (0.02 mm/s)). In contrast, in the sample which contained GF material, progressive columnar/equiaxed transition (PCET) was observed at v_{SL} = 0.077 mm/s and G_{SL} = 3.9 K/mm. The secondary (SDAS) dendrite arm spacing follows the well-known power law, $SDAS = K[t_0]^{\frac{1}{3}}$, where K is a constant, and t_0 is the local solidification time for both GB and μg experiments.

Keywords: Al-7 wt% Si; solidification; space; ground; grain structure; eutectic; secondary dendrite arm spacing

Citation: Roósz, A.; Rónaföldi, A.; Li, Y.; Mangelinck-Noël, N.; Zimmermann, G.; Nguyen-Thi, H.; Svéda, M.; Veres, Z. Microstructure Analysis of Al-7 wt% Si Alloy Solidified on Earth Compared to Similar Experiments in Microgravity. *Crystals* **2022**, *12*, 1226. https://doi.org/10.3390/cryst12091226

Academic Editors: Maria Cecilia Poletti, Silvana Sommadossi and Ricardo H. Buzolin

Received: 31 July 2022
Accepted: 23 August 2022
Published: 31 August 2022

1. Introduction

In the automotive industry, a large amount of Al-Si alloy is used. Among the significant Al-Si alloys is the hypoeutectic Al-7 wt% Si alloy (similar to the A357 alloy) with some minor other elements (Fe, Mn, Mg). From this alloy, the used automotive components are produced by a casting process. The mechanical properties of the casting products strongly depend on the microstructure.

The solidification of this alloy starts with the nucleation of the Al solid solution. The type of nucleation can be homogenous or heterogenous depending on whether the alloy

contains or does not contain any grain refinement. After that, Al solid solution cells or dendrites and finally Al-Si eutectic solidify. So, the microstructure of the solidified alloy consists of a dendritic network (aluminum solid solution) surrounded by Al-Si eutectic. During the solidification of this alloy, the density of the melt can change as the effect of concentration and temperature differences. At the solid /liquid (S/L) front (Figure 1), the concentration of the melt is the same as the basic alloy (C_0), and the temperature is the same as the liquidus temperature, TL, neglecting the undercooling of the solid/liquid front, which is only some °K in the practice of the casting. At the root of the dendrite (eutectic/liquid front, E/L), the concentration of the melt is the eutectic concentration, C_E, and the temperature is the eutectic temperature, TE, neglecting again the undercooling of the eutectic.

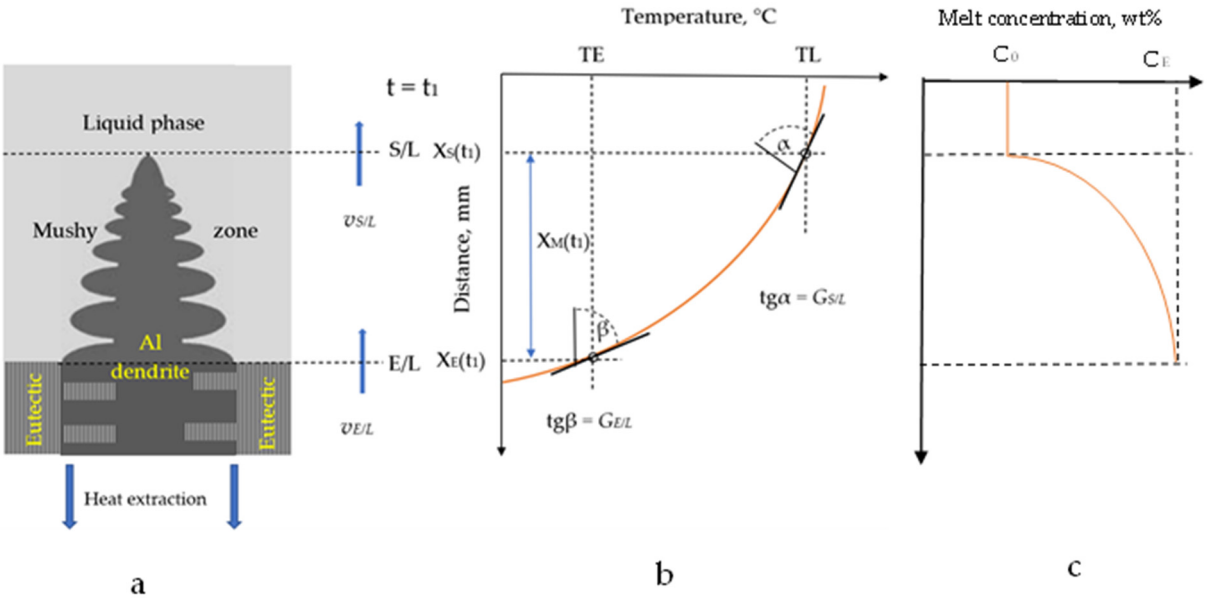

Figure 1. Sketch of the solidifies part of sample (**a**), temperature (**b**), and melt concentration (**c**) distribution in the mushy zone, with the solidification fronts (S/L, E/L), fronts position ($X_S(t_1)$, $X_E(t_1)$) *and* lengths of the mushy zone ($X_M(t_1)$ vs. time), front velocities ($v_{S/L}$, $v_{E/L}$), temperature gradients at the fronts, ($G_{S/L}$, $G_{E/L}$) in an arbitrary t_1 time.

During ground-based solidification, buoyancy flow can develop by the density difference mentioned above [1,2]. The buoyancy flow can affect the above issues: thermal field, solute distribution in the melt, and the position and amount of the new grains [3–7]. The buoyancy flow results can change the micro- and macro-segregation [8–11]. The buoyancy flow can affect the form of the solid/liquid front. It would be planar or cellular without melt flow at a high temperature gradient and a low velocity at the S/L front. In contrast, it would be dendritic at a low-temperature gradient and a high solid/liquid front velocity. Also, the buoyancy flow can significantly affect the columnar/equiaxed transition (CET) by three effects:

(i) The melt flow ahead of the S/L front can change the temperature and the concentration fields (the temperature and concentration gradients), parameters which determine the nucleation and the growth of the S/L front [12].

(ii) The interdendritic melt flow can break the secondary dendrite arms partly mechanically and partly due to the solute pile-up or transport of hot melt to the secondary arms remelting the neck of those [13,14]. These fragments are transported from the S/L front to the melt ahead of the front into the undercooled melt. Some part of those remelts, while the other parts grow and hinder the development of the columnar S/L fronts. If the volume fraction of the new grains reaches 50%, they can mechanically block the development of the columnar S/L front. After that, the grain structure will be equiaxed [14,15].

(iii) If the alloy contains grain refinement, the flow can move the particle of the grain refinement and can affect the CET [16–18].

The secondary dendrite arm spacing (SDAS, λ_2) of the hypoeutectic Al–7% Si cast alloy is one of the most important microstructural parameters since their mechanical properties strongly depend on the SDAS. The SDAS can change during solidification by coarsening [19–23]. The coarsening of the secondary dendrite arm is a diffusion process. The bigger arms can grow, and the smaller arms disappear [24,25]. Therefore, the SDAS increases during solidification. The interdendritic melt flow, overlapped with the diffusion, can accelerate the coarsening, and increase the (SDAS). Therefore, the SDAS changes during solidification. At the end of solidification, the SDAS is:

$$\lambda_2 = K(t_0)^n \quad (1)$$

where K is a constant of a given alloy, t_0 is the local solidification time, and n is the kinetic constant.

Suppose the coarsening is a pure diffusion process, $n = 1/3$ [19–25]. If the interdendritic flow is strong enough, the type of coarsening will be "convective", and the value of n will change from $1/3$ to $\frac{1}{2}$ [25].

As solidification is a very complex process, it isn't very easy to separate the different effects. Under microgravity conditions, natural convection does not exist or is strongly damped due to the absence of buoyancy force. Therefore, experiments in microgravity conditions provide unique benchmark data for purely diffusive solidification conditions. Within the CETSOL (columnar to equiaxed transition in solidification processes) project, four microgravity experiments (B2F1, B2F2, B2F5, and B2F6) [26] were performed in the solidification quench furnace (SQF) and one experiment (FM) was carried out in the low gradient furnace (LGF) on the International Space Station (ISS) [27]. These experiments were presented in detail in [26–32].

A very efficient approach to determine the buoyancy flow effect on the microstructure is to compare space experiments with similar experiments carried out on Earth. For this purpose, four ground-based experiments (GB1, GB2, GB5, and GB6) were performed with parameters similar to the space experiments. Even if the experiments were not performed in the same solidification equipment as the experiments in microgravity, and therefore the solidification parameters are not the same but similar, the results of space and ground-based experiments can be compared. This paper aims to compare the grain structure (especial the CET) and the type of the coarsening process of the secondary dendrite arm (especially the kinetic constant n) of the samples solidified in space and the Earth to get information on the effect of buoyancy flow on those.

2. Materials and Methods

2.1. Alloy

Grain refined and non-grain refined Al-7 wt% Si alloy was provided by Hydro Aluminium Rolled Products GmbH for the CETSOL project. The alloy was made from high-purity 99.99 wt% Al and 99.99 wt% Si material using a vacuum metallurgy process. An addition of 0.5 wt% master alloy AlTi5B was used for grain refinement.

2.2. Furnace

The GB experiments were performed in a vertical Bridgman-type tube furnace having four heating zones. Around the furnace, there is a 2-pole magnetic inductor that can produce a rotating magnetic field (RMF). The details of the furnace and the inductor are presented in [33].

The space experiments were carried out onboard the ISS using the solidification and quenching furnace (SQF) with or without stirring by rotating magnetic field (RMF). The SQF furnace consists of hot and cold zones separated by an adiabatic zone. The details of the furnace and the inductor are presented in [26].

2.3. Sample and Sample Holder

For the GB experiments, the sample diameter was 8 mm, and the length was 100 mm (Figure 2). Sample (2) was inserted into an alumina capsule (3). The temperature distribution was measured at 13 points by K-type thermocouples (4). Each thermocouple was put into a groove on the surface of alumina capsules. The alumina capsule with thermocouples was placed in a quartz tube (5). At the bottom of the quartz tube, a cooling core from copper (6) was connected to the alumina capsule (3), which was immersed in a water tank to increase the unidirectional heat removal. Since the water removes the heat at the copper core wall, the wall temperature is lower than at the center. Accordingly, the sample temperature is also lower at the crucible wall. This radial temperature gradient is at the origin of the nonplanar solid/liquid interface, as is shown in Section 3.3.

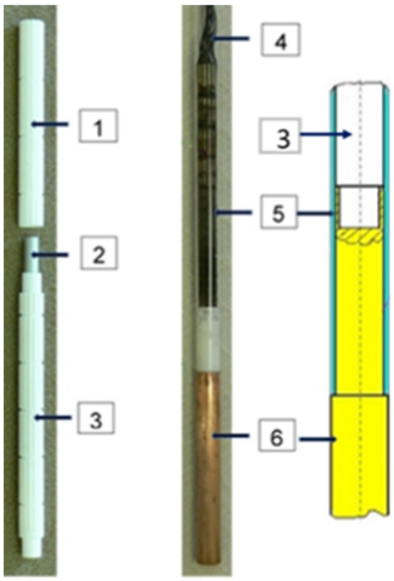

Figure 2. Ground experiments. Sample and crucible: (1) upper part of alumina capsule, (2) sample, (3) alumina capsule, (4) 12 K-type thermocouples, (5) quartz tube, (6) Cu cooling core.

For the microgravity experiments, the Al-7 wt% Si alloy samples (diameter: 8 mm, length 245 mm) were inserted into Al_2O_3 tube crucibles. The temperature distribution along the crucible was measured during the whole experiment by thirteen thermocouples (TC1–TC13) located at the outer surface of the crucible. The distance between thermocouples was 20 mm. The details of the cartridge are described in [26].

2.4. Solidification Experiments

Four ground-based (GB) solidification experiments were carried out with different parameters (Table 1a). The sample moving velocity (v_1) in Stage I was 0.02 mm/s, the same as in the B2F space experiments (Table 1b). The z_1 length of Stage I was 50 mm in contrast to the B2F samples, where z_1 was only 20 mm, so the steady-state solidification conditions were obtained in Stage I for GB experiments. In Stage II, the moving velocity of GB1 and GB2 samples was 0.2 mm/s, the same as for B2F1 and B2F2 experiments, and it was 0.02 mm/s for GB5 and GB6 experiments, the same as for the B2F5 and B2F6 samples. The z_2 length was longer (60 mm) than the B2F samples (50 mm). The ground-based samples were not quenched at the end of solidification, contrary to the space samples.

Table 1. (a). Parameters of GB experiments. (b) Parameters of B2F, FM space, and GM ground experiments.

(**a**)

Sample	Alloy	Initial G K/mm	Stage I		Stage II		
			v_1 mm/s	z_1 mm	v_2 mm/s	z_2 mm	RMF
GB1	Al + 7 wt% Si + GR	4	0.02	50	0.2	60	No
GB2	Al + 7 wt% Si	4	0.02	50	0.2	60	0.5 mT
GB5	Al + 7 wt% Si + GR	4	0.02	50	0.02	60	No
GB6	Al + 7 wt% Si	4	0.02	50	0.02	60	0.5 mT

(**b**)

Sample	Alloy	Initial G K/mm	Stage I		Stage II			
			v_1 mm/s	z_1 mm	v_2 mm/s	z_2 mm	R K/s	RMF
B2F1	Al + 7 wt% Si + GR	4	0.02	20	0.2	50	0.133	No
B2F2	Al + 7 wt% Si	4	0.02	20	0.2	50	0.133	0.5 mT
B2F5	Al + 7 wt% Si + GR	4	0.02	30	0.02	50	0.133	No
B2F6	Al + 7 wt% Si	4	0.02	30	0.02	50	0.133	0.5 mT
B1FM5/GM	Al + 7 wt% Si + GR	0.9	0.01	20	0.01	20	0.067	No

One pair of space (B1FM5) and ground (GM) experiments were carried out in the low gradient furnace (LGF) on the International Space Station (ISS). The solidification parameters were the same (Table 1b) for the two samples [29].

Before the solidification phase started, a thermal homogenization for 1800 s for all four GB samples was applied, much shorter than for B2F1, B2F2 samples (28,000 s), and B2F5, B2F6 samples (14,000 s).

The temperature of the upper heaters of the SQF furnace used for the microgravity experiments was cooled down with 0.133 K/min in stage II to decrease the temperature gradient. In contrast, the temperature gradient of our furnace was constant during Stage II. The GB2 and GB6 samples were stirred with RMF of 0.5 mT in Stage II, as with the B2F2 and B2F6 samples.

2.5. Microstructure Characterization

2.5.1. Preparation of the Samples

The samples were mounted into resin and cut along longitudinal and cross-sections. After wet grinding and polishing, the samples were etched in a 2% H.F. water solution to measure the secondary dendrite arm spacing (SDAS) and the amount of eutectic. After that, they were etched by Barker's solution to investigate the grain structure.

The positions of the investigated cross-sections from the bottom of the samples were as follows (Table 2) 0, 5, 15, 25, 45, 60, and 80 mm.

2.5.2. Measuring Methods

The quantitative metallography measurements (see below) were performed on the Zeiss AxioImager light microscope images.

Grain Structure

The grain number was determined on all cross-sections as follows: the grains were drawn around by hand and counted manually (Table 4a). The length/width (L/W) ratio was determined on the longitudinal section similarly: the grains were drawn around by hand, and the maximal length was measured perpendicular to each other manually.

Secondary Dendrite Arm Spacing (SDAS)

The longitudinal section of the samples was divided into 35 parts along the sample axis. The thicknesses of each part were 2.85 mm and 8 mm along and perpendicular to the sample axis. 200 SDAS values were measured in all parts. A line was laid across the

secondary arms (perpendicular to them, longitudinal with the primary dendrite arms), and the number of crossings was counted manually.

Al-Si Eutectic

The eutectic percentage was measured using a quantitative metallography method. The optical microscopy images of longitudinal sections of samples are segmented into binary images using a threshold to separate the two microstructure elements: the dendrite phase and eutectic appear in white and black, respectively. Based on those binary images, the eutectic volume percentage (E%) was measured in 20 places in all 35 parts.

Table 2. (a) The solidification parameters of GB samples at the investigated cross and longitudinal sections. (b) The solidification parameters of B2F samples at the investigated cross and longitudinal sections [31].

(a)											
No. Section	**Distance from the Bottom of Samples, mm**	**Part**		**S/L Temp. Gradient, G_{SL}, K/mm**				**S/L Front Velocity, v_{SL}, mm/s**			
		GB1 GB2	**GB5 GB6**	**GB1**	**GB2**	**GB5**	**GB6**	**GB1**	**GB2**	**GB5**	**GB6**
1	0	1	2/2								
2	5	2	3/2								
3	15	3	4/3	4.65	4.59	4.58	4.98	0.011	0.009	0.12	0.014
4	25	3	5/3	3.59	3.45	3.64	3.85	0.021	0.022	0.016	0.018
5	45	4	5/5	3.53	3.49	3.82	3.77	0.041	0.044	0.019	0.020
6	60	5	5/5	4.2	4.31	3.56	3.36	0.109	0.110	0.023	0.024
7	80	5	5/5	4.03	3.87	2.93	2.34	0.181	0.176	0.025	0.027
(b)											
No. Section	**Distance from the Bottom of Samples, mm**	**Part**		**S/L Temp. Gradient, G_{SL}, K/mm**				**S/L Front Velocity, v_{SL}, mm/s**			
		B2F1/ B2F2	**B2F5/ B2F6**	**B2F1**	**B2F2**	**B2F5**	**B2F6**	**B2F1**	**B2F2**	**B2F5**	**B2F6**
1	135	5	5	5.18	5.23	4.26	4.45	0.062	0.069	0.017	0.016
2	165	6	6	-	12.32	3.34	3.27	-	1.39	0.53	0.054
3	195	7	6	-	8.83	2.60	2.68	-	0.39	0.072	0.074
4	225	7	6	-	8.54	1.93	1.89	-	1.12	0.096	0.088

3. Results of GB Experiments

The solidification process of the samples is characterized by the velocities ($vs_{/L}$, $v_{E/L}$) and the temperature gradients ($G_{S/L}$, $G_{E/L}$) of the liquidus (S/L) and eutectic (E/L) fronts (at the liquidus (TL) and eutectic (TE) temperature, respectively, as a function of time (equivalent to position along the sample). The sketch of a part of the sample during solidification, the front positions, the velocities, and the temperature gradients can be seen in Figure 1 at an arbitrary $t = t_1$ time.

3.1. Cooling Curves

The temperature (cooling curve) was measured by 13 thermocouples (Figure 3, TC1–TC13). During the analysis, it was supposed that the undercooling of the primary dendrite tips and eutectic could be neglected. It means that the solidification starts at the liquidus temperature (TL) and is completed when the eutectic temperature (TE) is reached. The details of the analysis were presented in an earlier paper [31], and the calculated velocities as a function of the position in the sample (length from the bottom of the sample) can be seen in Figure 4 for the ground experiments.

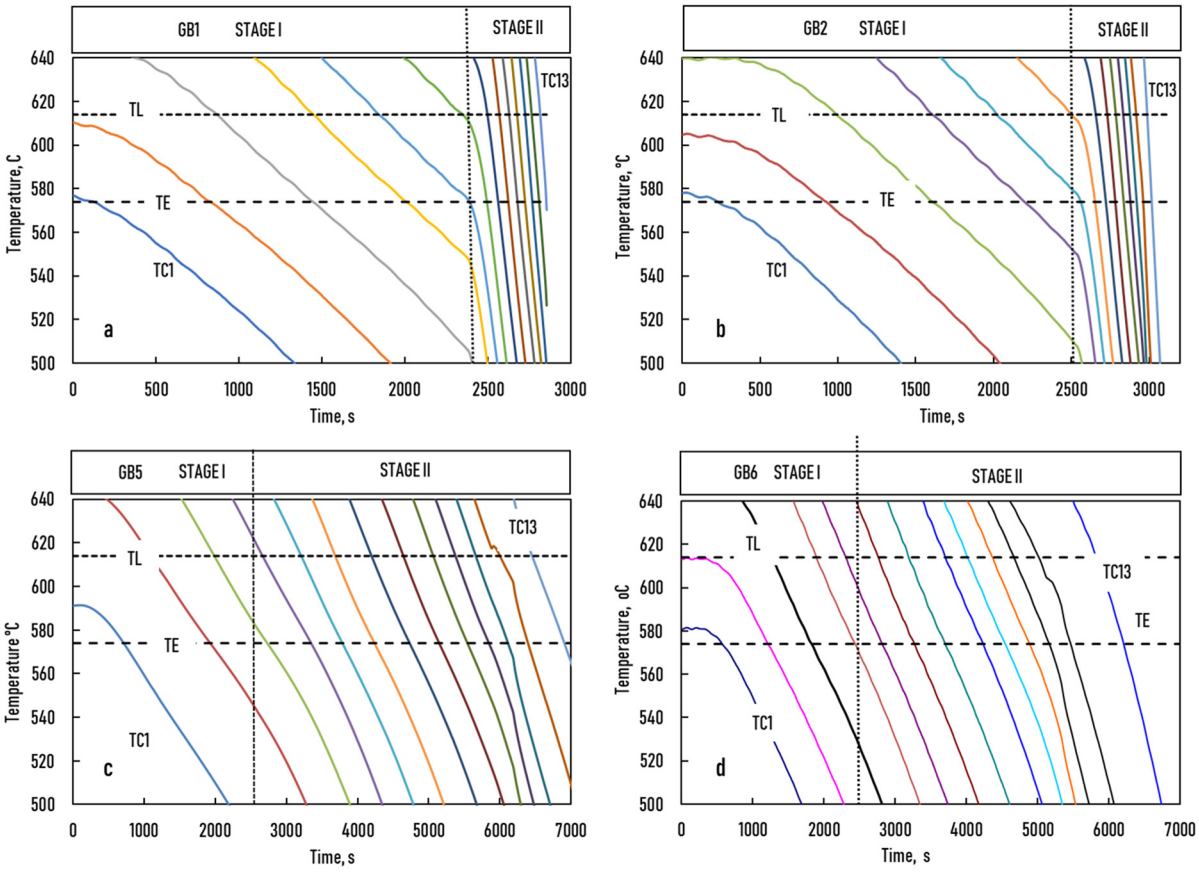

Figure 3. The measured cooling curves at different places by TC1 – TC13 thermocouples of the four ground experiments (**a**): GB1, (**b**): GB2, (**c**): GB5, (**d**): GB6. The different colours mean the data measured by different thermocouples.

3.2. Front Velocities and Temperature Gradients

In Stage I, the four GB samples moved 2500 s long at a velocity of 0.02 mm/s for a length of 50 mm, and in Stage II, 300 s at a higher velocity of 0.2 mm/s for a length of 60 mm (GB1 and GB2 samples) and 3000 s again at 0.02 mm/s for a length of 60 mm (GB5 and GB6 samples). The actual E/L and the S/L fronts velocity could not follow the pulling velocity of the sample given in Table 1a, and so they must be determined from sample cooling curves. In order to analyse the microstructure evolution along the sample, it is thus crucial to know exactly the variations of the solidification parameters as function of position.

3.2.1. The $v_{E/L}$, $v_{S/L}$ Front Velocities and the $G_{E/L}$, $G_{S/L}$ Temperature Gradients for GB1 and GB2 Samples

For GB1 and GB2, the two differences were (i) the addition of grain refiners in GB1 and (ii) applying an RMF during Stage II for the GB2 non-refined sample. Both differences have negligible influence on the isotherm velocities, so that the calculated velocities of the S/L and E/L fronts are very similar in both samples, as visible in Figure 4a,b. The calculated average velocities are also shown in the figures since they were used to calculate the SDAS later (see Section 3.6).

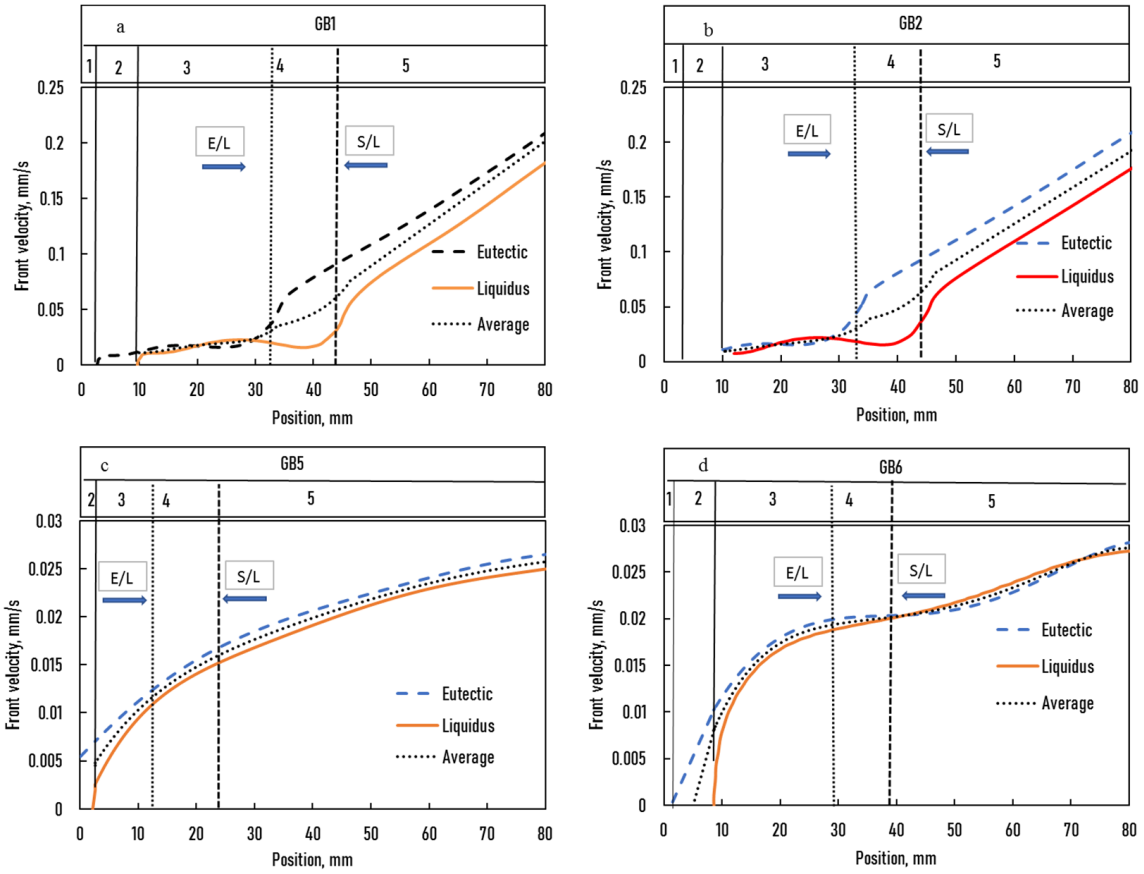

Figure 4. Velocities of the S/L and E/L fronts vs. position for the four ground samples (**a**): GB1, (**b**): GB2, (**c**): GB5, (**d**): GB6.

At t = 0 s, the E/L, and S/L fronts were at 2 and 10 mm (initial mushy zone), respectively. From the $X_E(t)$ and $X_L(t)$ function (X_E and X_L are the positions of the E/L and S/L fronts at time t) at 2500 s (Stage II, at the change of the sample moving velocity), the E/L and S/L fronts were 33 mm (dotted line) and 44 mm (dashed line) in Figure 4a,b), respectively.

The samples were divided longitudinally into five parts for which the solidification process differed, such as the B2F1 and B2F2 samples presented in [31]. Part 1 was not melted. Part 2 was the initial mushy zone, where the samples were partly melted. During solidification, only the E/L front moved. In Part 3, the velocity of the two fronts was nearly the same, close to the lowest velocity (0.02 mm/s). In Part 4, the $v_{E/L}$, increased while $v_{S/L}$ remained low. In Part 5, both velocities increased until the higher velocity (0.2 mm/s). The $v_{S/L}$ remained lower with a constant value of 0.04 mm/s. In the case of the GB2 sample, the RMF was switched on in Part 5.

The temperature gradients $G_{E/L}$, $G_{S/L}$ are similar except in Part 4 and the start of Part 5, where the two front velocities are very different. Both temperature gradients decrease strongly in Parts 2 and 3 (Figure 5a,b).

The velocities and temperature gradients changing in the different Parts are shown in Table 3a in detail.

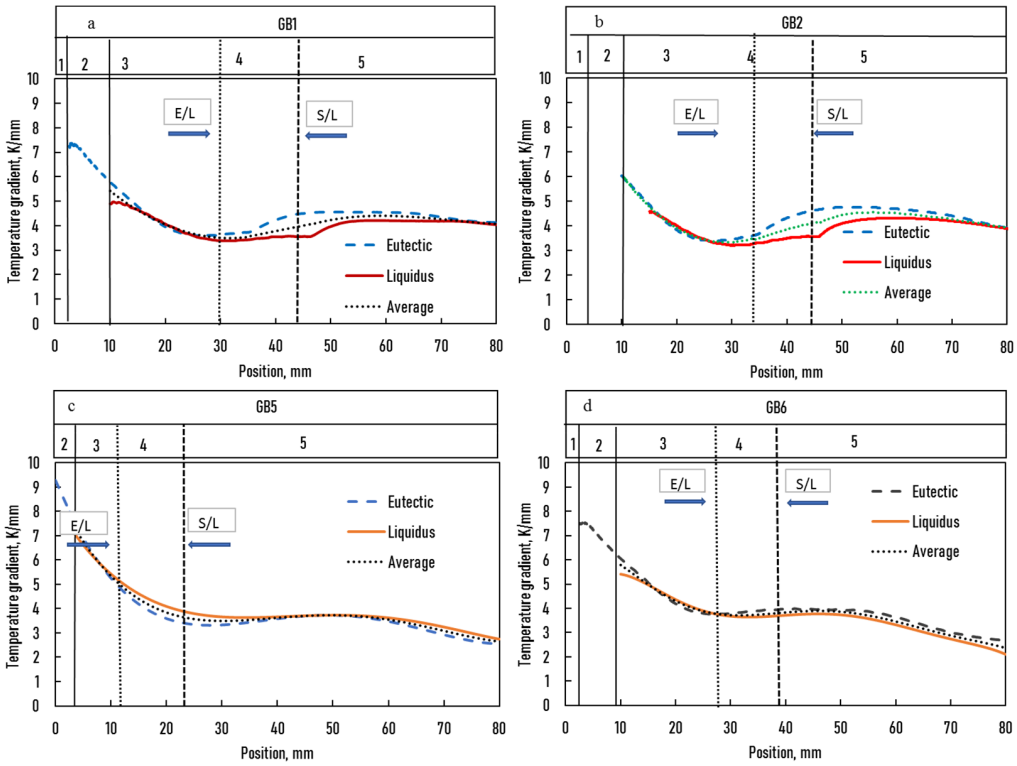

Figure 5. Temperature gradient at the S/L and E/L fronts vs. position of four samples (**a**): GB1, (**b**): GB2, (**c**): GB5, (**d**): GB6.

3.2.2. The $v_{E/L}$, $v_{S/L}$ Front Velocities and the $G_{E/L}$, $G_{S/L}$ Temperature Gradients for GB5 and GB6 Samples

Similar to GB1 and GB2, for GB5 and GB6, the two differences were also (i) the addition of grain refiners in GB5 and (ii) the application of an RMF during Stage II for the GB6 non-refined sample. Both differences have negligible influence on the isotherm velocities. The calculated velocities of the S/L and E/L fronts were something different for the samples, as visible in Figure 4c,d. The calculated average velocities are also shown in the figures since they were used to calculate the SDAS later (see Section 3.6).

At t = 0 s, the E/L fronts were at −6 mm (GB5, virtually, under the sample) and 2 mm (GB6). The S/L front was at 2 mm (GB5) and 9 mm (GB6) (initial mushy zone). From the $X_E(t)$ and $X_L(t)$ function at 2500 s (at the beginning of Stage II where the RMF was switched on), the E/L front was 13 mm (GB5), and 28 mm (GB6) (dotted line) and the S/L front was 24 mm (GB5) and 39 mm (GB6) and 43.75 mm (dashed) line in Figure 4c,d), respectively.

The samples were divided longitudinally into four (GB5) and five (GB6) relevant parts, during which the solidification process was different. Part 1 was not melted only in the case of GB6 since, in the case of GB5, the thermal field was shifted to the direction of the bottom of the sample. Part 2 was partly remelted (initial mushy zone), where only the E/L front moved. In Part 3, the velocity of the two fronts increased; in Part 4 and 5, the two velocities were nearly the same and increased continuously. At 80 mm, the velocities are slightly higher (0.025 mm/s) than the sample moving velocity (~0.025 mm/s). The cause was that the amount of the melt at the end of solidification decreased, while the amount of removed heat was constant. This effect was visible at the GB1 and GB2 also, but only after 80 mm, so it is not in Figure 4a,b. The temperature gradients $G_{E/L}$, *and* $G_{S/L}$ are nearly the same for the two samples. Both temperature gradients decrease strongly in Part 3 and 4 (GB5) in Part 3 (GB6) (Figure 5c,d). The velocities and temperature gradients changing in the different parts are shown in Table 3b in detail.

Table 3. (a). The velocities and temperature gradients changing in the different Parts of GB1 and GB2 samples. (b). The velocities and temperature gradients changing in the different Parts of GB5 and GB6 samples.

(a)						
Position of the E/L and S/L fronts at change of Stage	GB1, GB2	E/L front	33 mm			
		S/L front	44 mm			
		Part 1	**Part 2**	**Part 3**	**Part 4**	**Part 5**
		not melted part	partly melted part	fully melted part	fully melted part	fully melted part
Distance, mm	GB1, GB2	from 0 to 2	from 2 to 10	from 10 to 33	from 33 to 44	from 44 to 80
$v_{E/L}$, mm/s	GB1, GB2	-	incr. from 0.0 to 0.011	incr. to 0.02	incr. to 0.09	incr. to 0.25
$v_{S/L}$, mm/s	GB1, GB2	-	S/L front isn't exist	incr. from 0.0 to 0.022	incr. to 0.029	incr. to 0.22
$G_{E/L}$, K/mm	GB1	-	decr. from 7.23 to 5.77	decr. to 3.58	incr. to 4.47	decr. to 4.13
	GB2	-	decr. from 7.0 to 6.21	decr. to 3.42	incr. to 4,56	decr. to 3.89
$G_{S/L}$, K/mm	GB1	-	S/L front isn't exist	decr. from 4.89 to 3.39	incr. to 3.54	incr. to 4.03
	GB2	-	S/L front isn't exist	decr. from 5.25 to 3.23	incr. to 3.56	incr. to 3.87
(b)						
Position of the E/L and S/L fronts at change of Stage	GB5	E/L front	13 mm			
		S/L front	23 mm			
	GB6	E/L fron	28 mm			
		S/L front	39 mm			
		Part 1	**Part 2**	**Part 3**	**Part 4**	**Part 5**
		not melted part	partly melted part	fully melted part	fully melted part	fully melted part
Distance, mm	GB5	isn't exist	from 0 to 2	from 2 to 13	from 13 to 23	from 23 to 80
	GB6	from 0 to 2	from 2 to 9	from 9 to 28	from 28 to 39	from 39 to 80
$v_{E/L}$, mm/s	GB5	-	incr. from 0.0054 to 0.0066	incr. to 0.011	Incr. to 0.015	incr. to 0.026
	GB6	-	incr. from 0.00 to 0.009	incr. to 0.0198	incr. to 0.02	incr. to 0.27
$v_{S/L}$, mm/s	GB5	-	S/L front isn't exist	incr. to 0.0096	incr. to 0.013	incr. to 0.025
	GB6	-	S/L front isn't exist	incr from 0.00 to 0.0187	incr. to 0.019	incr. to 0.27
$G_{E/L}$, K/mm	GB5	-	decr. from 9.30 to 7.21	decr. to 5.20	decr. to 3.63	decr. to 2.60
	GB6	-	decr. from 7.49 to 6.50	decr. to 3.76	incr. to 3.94	decr. to 2.68
$G_{S/L}$, K/mm	GB5	-	S/L front isn't exist	decr. from 7.2 to 5.44	decr. to 4.14	decr. to 2.93
	GB6	-	S/L front isn't exist	decr. from 5.6 to 3.66	incr. to 3.71	decr. to 2.34

3.3. Grain Structure

The grain and the dendritic structure of the GB samples can be seen in Figures 7 and 8. The centre of Figure 7b shows the grain structure variation along the whole sample. The 1–7 positions marked by white lines indicated where the cross and detailed longitudinal sections were made. The right column (c) of figures shows the grain structure on the cross-sections of samples, while the left column (a) depicts the dendritic structure on the typical area on the longitudinal section at the 1–7 position. The solidification parameters at the investigated cross-section can be seen in Table 3a for GB samples and Table 3b for B2F samples.

The original microstructure of the samples (Figure 6 and "A" in the bottom of Figures 7a,b,d and 8b) contains elongated aluminium (α) grains, which were coarsed at the

high temperature (some Kelvin below the eutectic temperature) during the melting of the sample in the not melted part. The particles of the Si phase of the eutectic are very fine in the original microstructure. Those remain inside the coarse α phase.

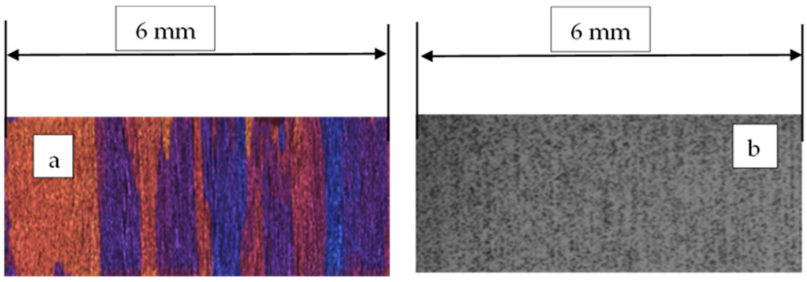

Figure 6. (**a**) Coarsened α grains in the non-melted part; (**b**) very fine Si particles in it.

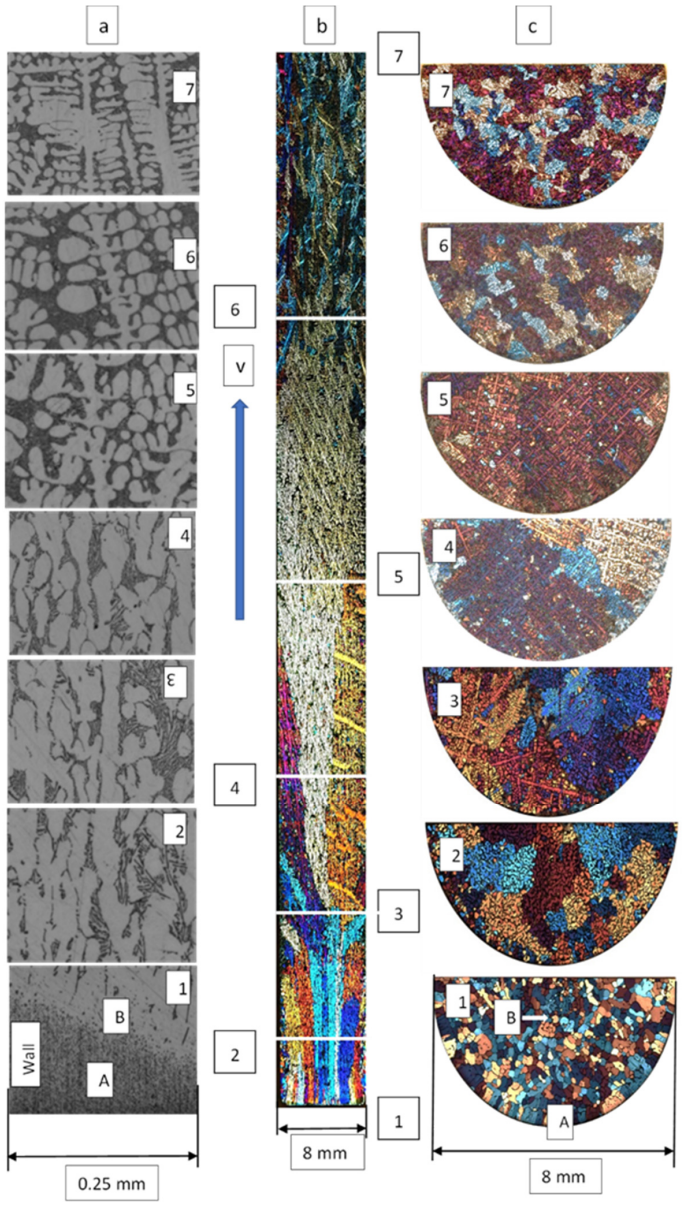

(**a**)

Figure 7. *Cont.*

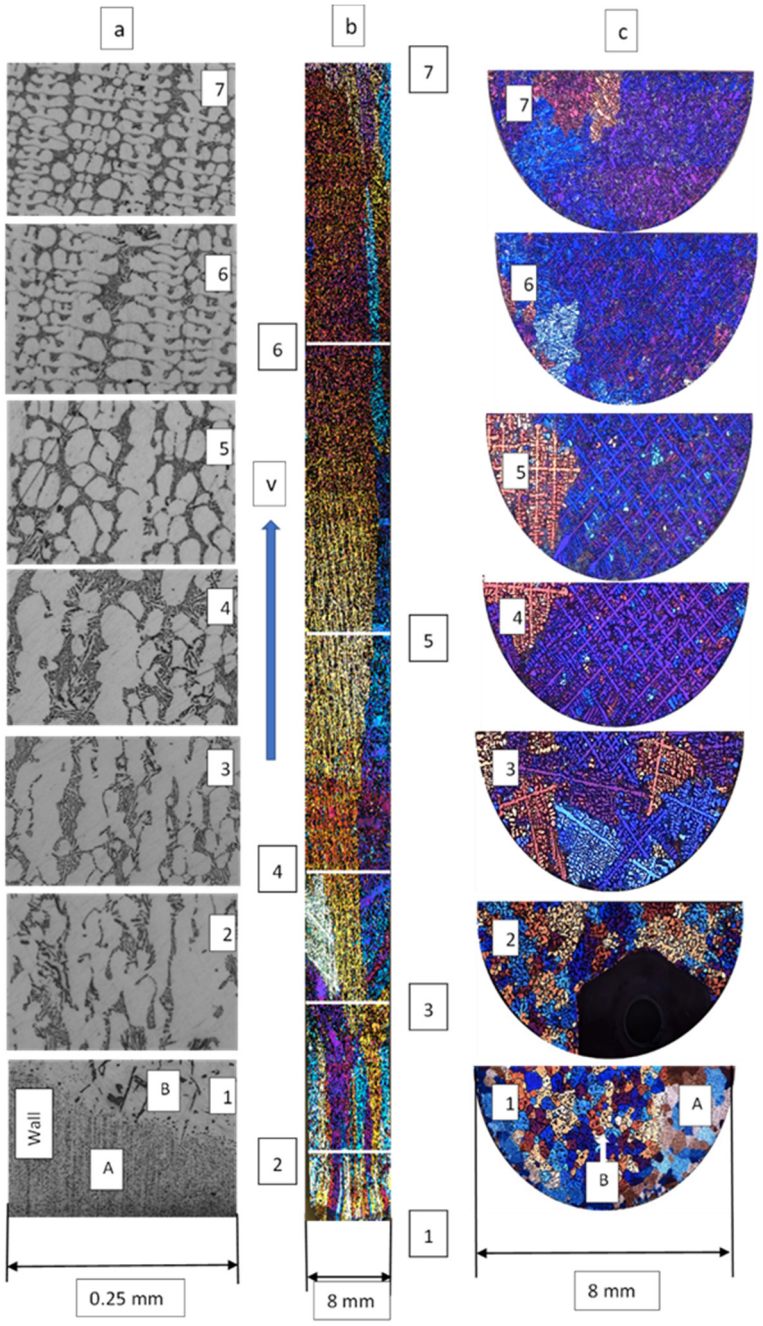

(**b**)

Figure 7. *Cont*.

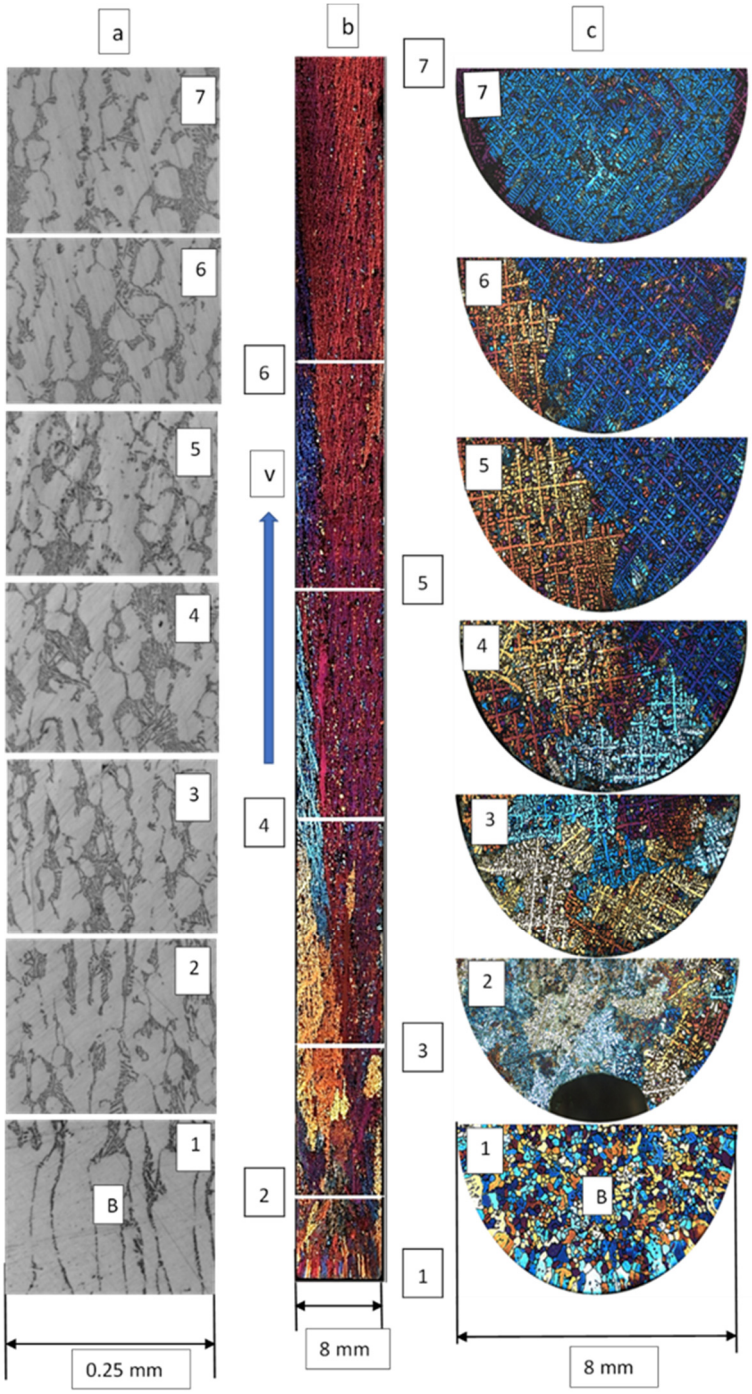

(**c**)

Figure 7. *Cont.*

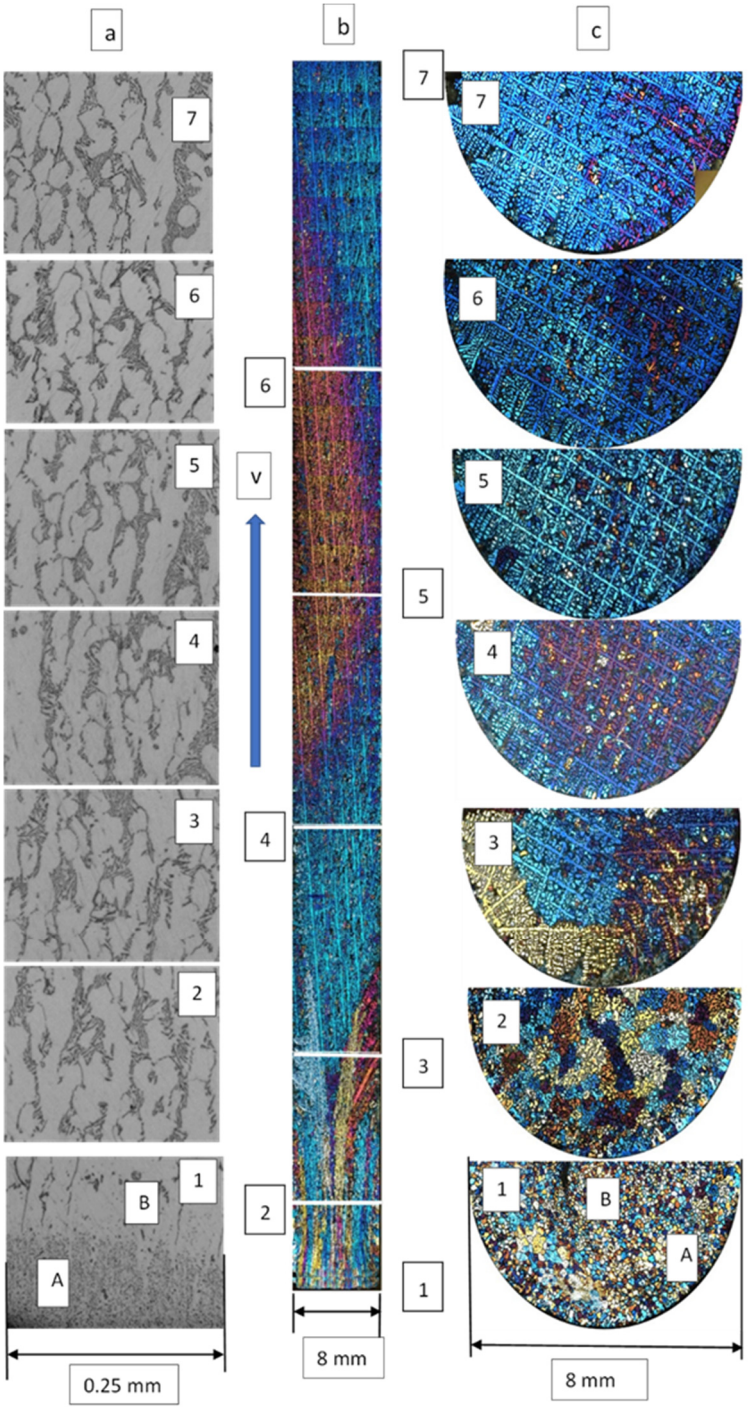

(**d**)

Figure 7. (**a**) Microstructure of Sample GB1-a: grain structure of the whole sample, longitudinal section; b: grain structure at the cross-section; c: dendritic structure at the longitudinal section; the blue arrow shows the direction of solidification. (**b**) Microstructure of Sample GB2; a: grain structure of the whole sample, longitudinal section; b: grain structure at the cross-section; c: dendritic structure at the longitudinal section; The blue arrow shows the direction of solidification. (**c**) Microstructure of Sample GB5; a: grain structure of the whole sample, longitudinal section; b: grain structure at the cross-section; c: dendritic structure at the longitudinal section; The blue arrow shows the direction of solidification. (**d**) Microstructure of Sample GB6; a: grain structure of the whole sample, longitudinal section; b: grain structure at the cross-section; c: dendritic structure at the longitudinal section; The blue arrow shows the direction of solidification.

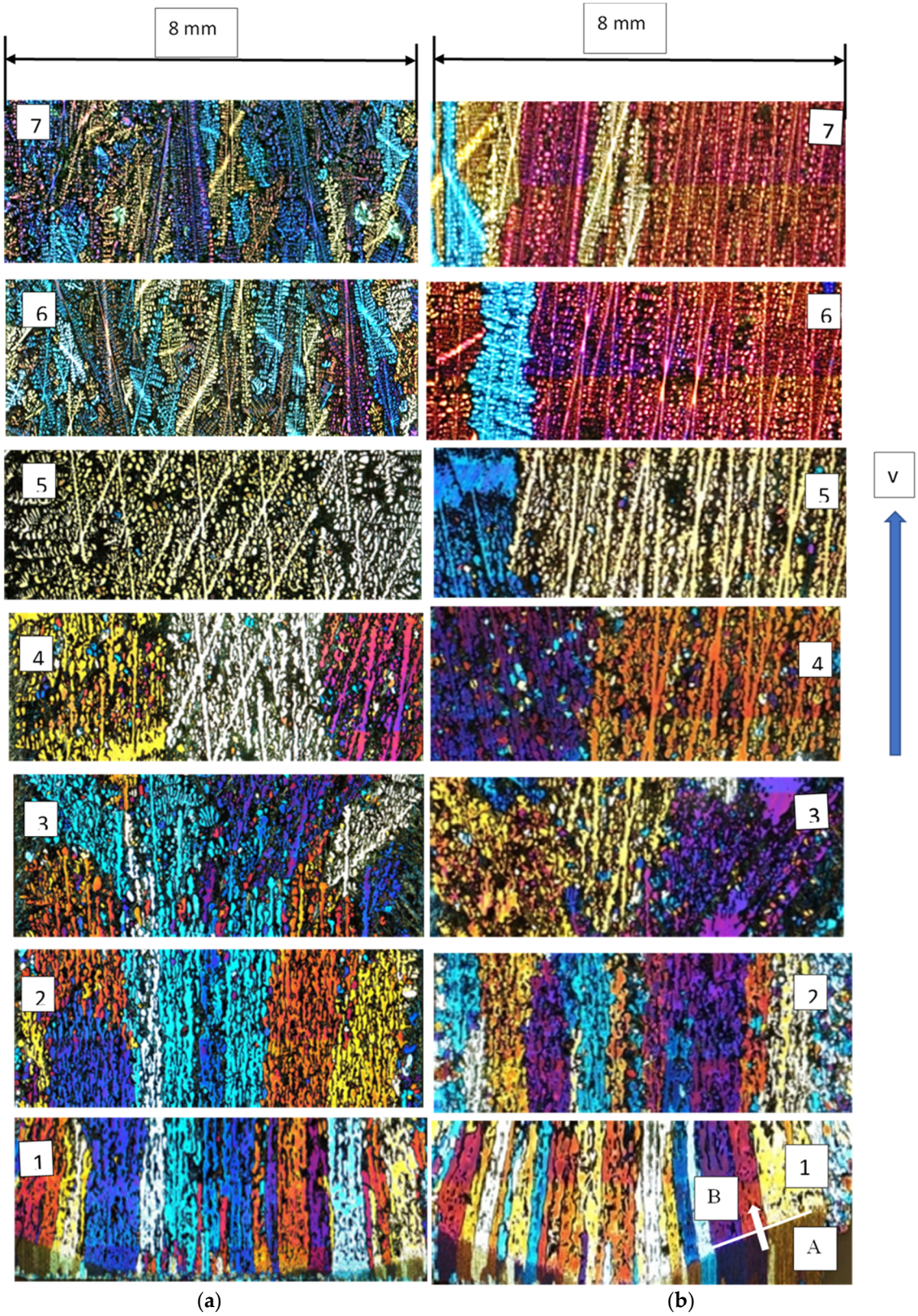

Figure 8. *Cont.*

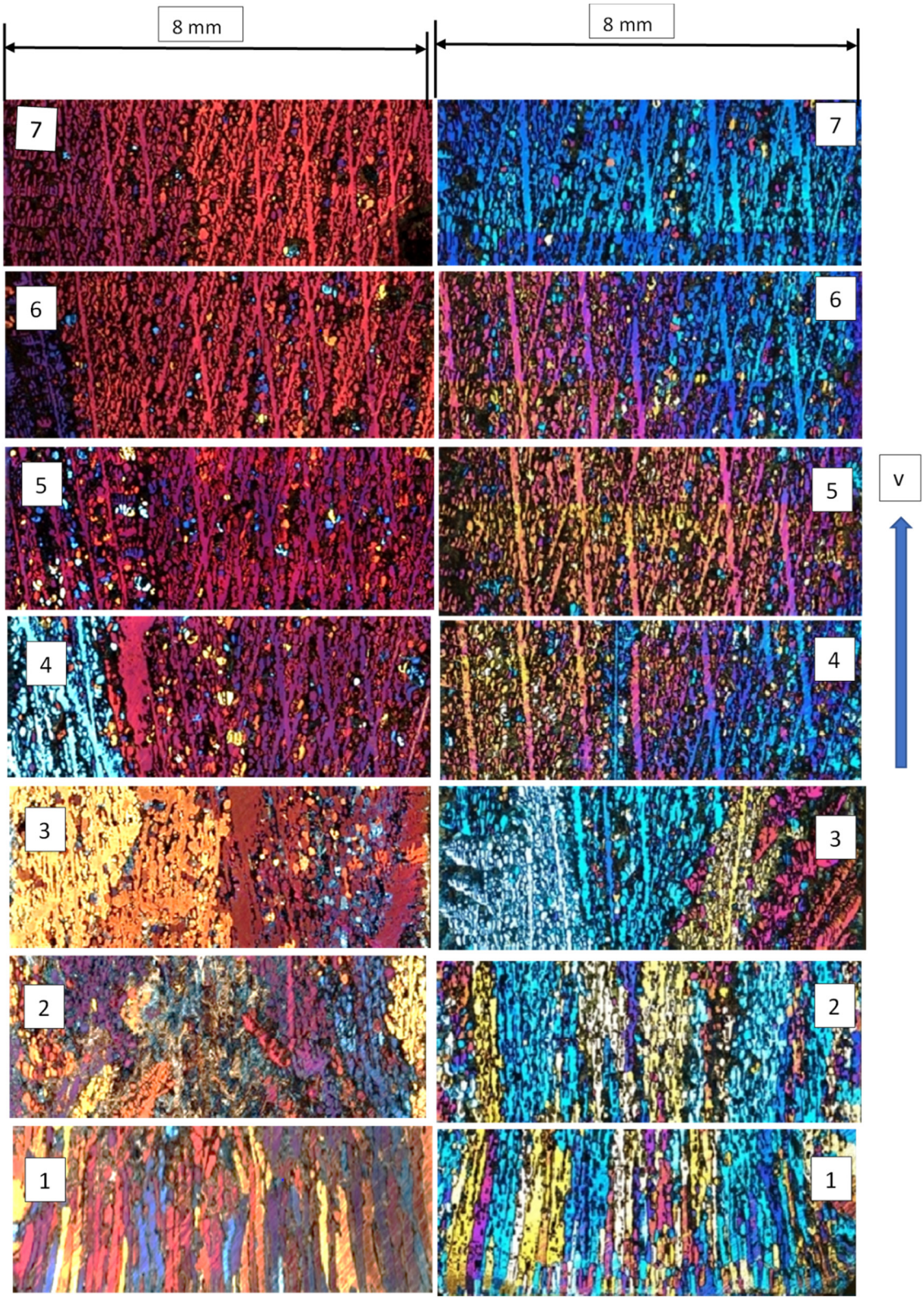

Figure 8. (**a**) Longitudinal section of Sample GB1 at cross section 1 to 7. The blue arrow shows the direction of solidification. (**b**) Longitudinal section of Sample GB2 at cross section 1 to 7. The blue arrow shows the direction of solidification. (**c**) Longitudinal section of Sample GB5 at cross section from 1 to 7. The blue arrow shows the direction of solidification. (**d**) Longitudinal section of Sample GB6 at cross section from 1 to 7. The blue arrow shows the direction of solidification.

Part 1

As it follows from the velocity of the eutectic front (see Figure 4), the first 2 mm of the samples were not melted in the case of Samples GB1, GB2, and GB6, while the GB5 hasn't not melted part.

Part 2: initial mushy zone

The cross and longitudinal image of Section 1 (c1 and a1 in Figure 7a,b,d) and the longitudinal image (1 in Figure 8a,b,d) show that near the crucible wall, the partly melted part of the samples begins far from the bottom of the sample ("A" in the Figures 7 and 8) than the centre of the samples ("B" in the Figures 7 and 8)

The boundary between the not melted and partly melted parts (the eutectic isotherm, white line in Figure 8b, image 1) is not perpendicular to the sample axis or crucible's wall. It means that the temperature was lower at the crucible wall (as mentioned before) than in the centre of the sample axis due to the intense heat extraction of the copper core near the crucible wall.

Past the eutectic temperature (ahead of the not melted/partly melted front), the eutectic (which takes up the ~50% of the microstructure in equilibrium) melted immediately, and with the increasing temperature, more and more α phase also melted. The new α grains, which solidified from the initial mushy zone, grew perpendicular to the not melted/partly melted boundary (white arrows in image 1, Figure 8b) with epitaxial growing. The Si phase appeared as two types of degenerated eutectic. The small Si particles and the α phase around those were melted, the formed small liquid drops coagulated and solidified in the α grains ("A" in Figure 9), and the other part solidified between the α grains ("B" in Figure 9).

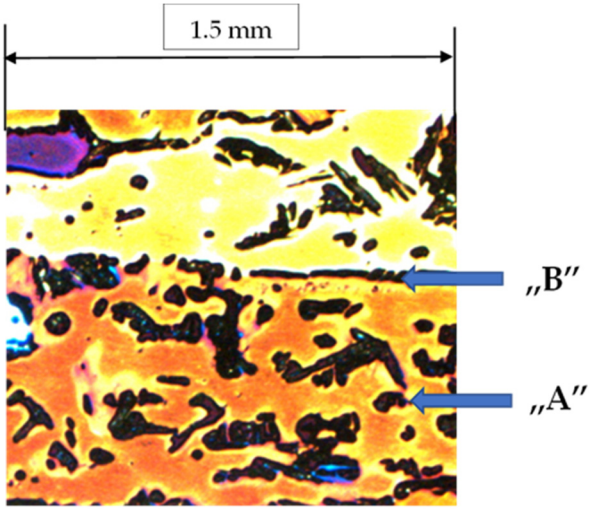

Figure 9. Two types of degenerated eutectic in the resolidified initial mushy zone sample GB2.

Section 2 is also in the initial mushy zone for GB1, GB2, and GB6. The liquid phase was more than in Section 1, so cellular microstructure developed (c2 in Figure 7a,b,d and 2 in Figure 8a,b,d) during solidification. Degenerated and equilibrium (two phases) eutectic solidified between the α phase (a2 in Figure 7a,b,d). Only a few cellular α grains remained from the grains of Section 1 and produced some new grains (c2 in Figure 7a,b,d and 2 in Figure 8a,b,d), which solidified unidirectionally. It must be noted again that the microstructure of Sections 1 and 2 developed during the solidification of the initial mushy zones (only the eutectic isotherm moved through the mushy zone), then the microstructure cannot be characterized by the solidification's parameters G_{SL} and v_{SL} only with the G_{EL} and v_{EL}.

Part 3

After the initial mushy zone (Section 3), some grains that developed in the initial mushy zone grew towards the fully melted part of the samples (c3 in Figure 7a,b,d, 3 in Figure 8a,b,d). The grain number is between 4 and 11 in the different samples, which are transient between the equiaxed and columnar grains (Table 4).

Table 4. (a). Measured grain number, GB samples; (b). Measured grain number, B2F samples.

(a)	**No. Cross Section/Distance from the Bottom of the Sample, mm**				
	3/15	**4/25**	**5/45**	**6/60**	**7/80**
GB1	5	3	5	93	117
GB2	11	3	2	5	6
GB5	10	5	2	2	1
GB6	4	3	1	1	1
(b)	**No. Cross Section/Distance from the Bottom of the Sample, mm**				
	1/135	**2/165**	**3/195**	**4/225**	
B2F1		38	547	732	
B2F2	12	15	54	32	
B2F5	19	14	24	7	
B2F6	10	7	3	6	

In the case of GB5, Section 2 was in Part3, which was fully melted, and equiaxed dendritic microstructure formed during solidification (c2 in Figure 7c and 2 in Figure 8c).

Between Sections 3 and 4, some (3–5) grains were selected during the growing (c4 in Figure 7 and 4 in Figure 8). The grains in which the primary dendrite arms grew almost parallel with the sample axis (in the direction of heat extraction) hindered the growth of the other grains. In this part of the samples, the E/L and S/L front velocity and the temperature gradient at the two fronts were nearly the same and increased from zero to 0.02 mm/s and decreased from 6 to 3 K/mm, respectively. In Section 4, the grain structure is columnar and similar in the case of the four samples, and there is no effect of the grain refinement.

Part 4

Between Sections 4 and 5, in the case of the samples GB1 and GB2, the S/L front velocity increased to 0.044 mm/s, and the temperature gradient at the S/L front decreased to 3.5 K/mm. These parameters determine the number of the grain and the columnar/equiaxed transition, CET. The grain structure remained columnar, but in the GB1, which contains grain refinement materials, the grain number was slightly more than in the GB2, which doesn't contain grain refinement materials (5 and 2) in Section 5 (c5 in Figure 7a,b and 5 in Figure 8a,b). The grain structure of samples GB5 and GB6 (Part 3) remained columnar, and the grain number decreased slightly (c5 in Figure 7a,b, and 5 in Figure 8a,b).

Part 5

Between Sections 5 and 6 in the sample GB1, some little equiaxed grain appeared between the columnar grains at ~50 mm (white circles in Figure 10a), where the v_{SL} and the G_{SL} at the S/L front were 0.074 mm/s and 3.96 K/mm, respectively (CET_{min}, point 1 in Figure 17a). At ~55 mm (v_{SL} = 0.093, G_{SL} = 4.19 K/mm), the number of equiaxed grains developed between the columnar grains is higher, and the diameter is larger (white circles in Figure 10b). In Section 6 (v_{SL} = 0.11 mm/s, G_{SL} = 4.2 K/mm), the sample consists of only elongated grains (b6 in Figure 7A and 6 in Figure 8a, point 2 in Figure 7a). The grain number is 93. From Section 6 to Section 7 the v_{SL} increased to 0.18 mm/s, G_{SL} remained 4.2 K/mm. The sample consists of more and more elongated grains, and in Section 7, the grain number is 117. The angle between the grains' longer axis (PDA's axis) and the sample's axis (the direction of heat extraction) is almost 0–30°. The grains' length (L) and width (W) were measured on the longitudinal section of the sample, and the elongation factor EF = L/W was calculated from those. The results are shown in Figure 11. If the EF is above 2.0, the grain is columnar [15], then about ~20% is quite equiaxed, but ~80% is so-called elongated equiaxed.

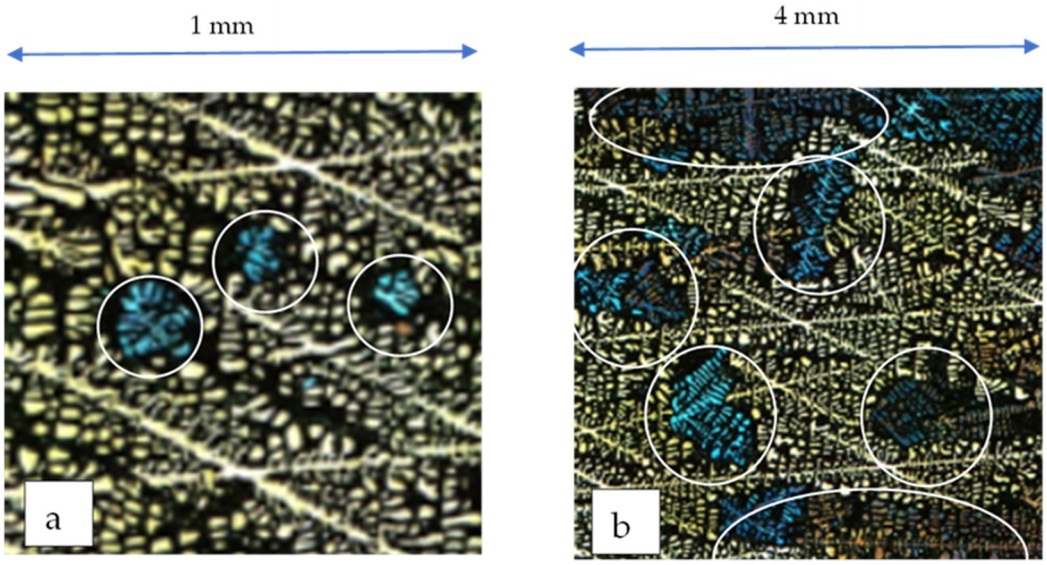

Figure 10. Equiaxed grains between the columnar grains; Length from bottom of sample (**a**) 50 mm; (**b**) 55 mm.

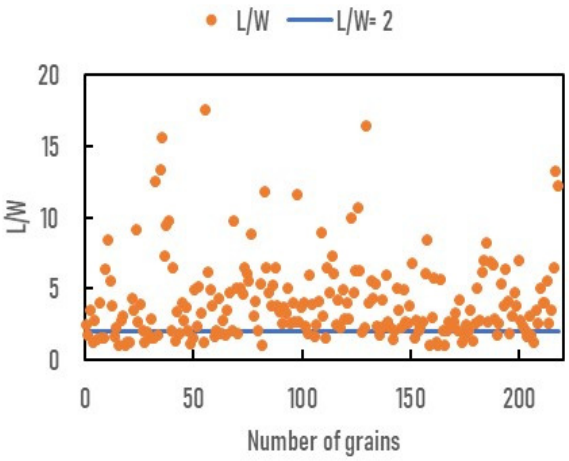

Figure 11. Length/width of the 250 grains between the cross Sections 6 and 7 in the sample GB1.

The grain structure of the sample GB2 remained columnar, and the grain number is 5, a little more than in Section 5. The RMF steering with 0.5 mT magnetic induction, which was switched on in this part of the GB2 sample, hasn't affected the grain structure. The cause of this change is the increase in the S/L front velocity.

The grain structure of the samples GB5 and GB6 didn't change between Sections 6 and 7, it remained columnar. The v_{SL} increased from 0.022/0.023 mm/s to 0.025/0.027 mm/s, and G_{SL} decreased from 3.56/3.36 K/mm to 2.93/2.34 K/mm (GB5/GB6). The cooling rate ($v_{SL}G_{SL}$) decreased from ~0.08 K/s to ~0.063 K/s. In Section 7 is only 1 grain. The RMF steering with 0.5 mT magnetic induction, switched on in this part of the sample GB6, has not affected the grain structure.

3.4. The Relative Amount of Eutectic and the Si Concentration Distribution

Figure 14 shows the measured volume% of eutectic ($E_{meas}(v\%)$) as a function of position in the four samples. Based on the equilibrium phase diagram, the theoretical equilibrium amount of the Al-Si eutectic is $E_{eq}(wt\%)$ = 48.5 wt%. Knowing that the densities of Al (2700 kg/m^3) and Si (2329 kg/m^3) are close to each other, the equilibrium volume percentage of eutectic was calculated $E_{eq}(v\%)$ = 51.8 vol% and is represented as a straight line in Figure 12. The average measured values $E_{av}(v\%)$ for four samples are less than equilibrium. The reasons for it could be explained by the formation of degenerate eutectic between the

secondary dendrite arms [33,34]. The average $E_{av}(v\%)$ of the samples must be equal to the 51.8%, so a correction factor ($K_C = E_{eq}(v\%)/E_{av}(v\%) = 1.25$) was calculated. Additionally, assuming that the rate of the degenerated eutectic was the same in the whole sample, the eutectic amount, $E_{rec}(v\%) = 1.25 \times E_{meas}(v\%)$, was recalculated with the correction factors as was earlier in [31] (Figure 12). The grain refinement material (GB1 and GB5) and the stirring by 0.5 mT (GB2 and GB6) didn't affect the amount of eutectic.

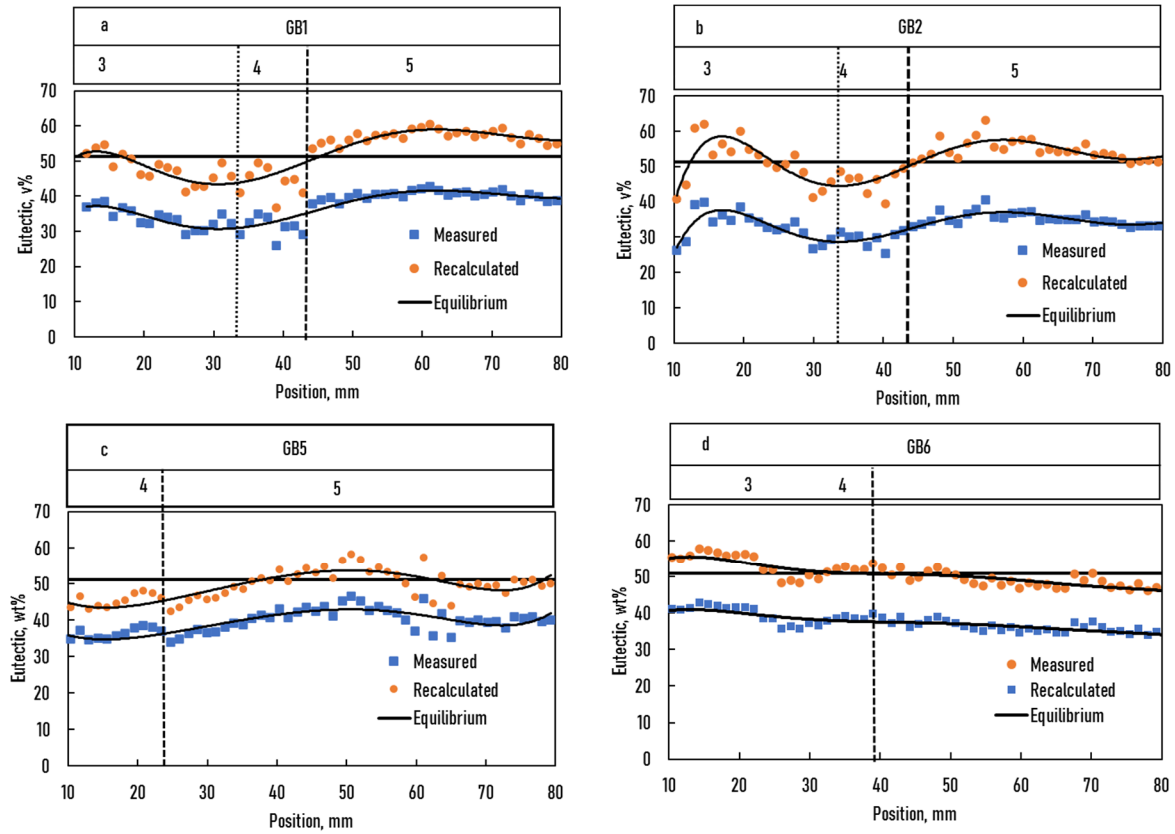

Figure 12. Measured, equilibrium, and recalculated amount of the eutectic vs. position in the sample: (**a**): GB1, (**b**): GB2, (**c**): GB5, (**d**): GB6.

The Si weight concentration (C_{Si}) was calculated as follows:

$$E(wt\%) = \frac{\rho_{eut}\ K_c\ E_{rec}(v\%)}{(\rho_{eut}\ K_c E_{rec}(v\%)) + \rho_\alpha(100 - K_c E_{rec}(v\%))} \quad (2)$$

$$C_{Si} = E(wt\%)(C_E - C_{\alpha,max}) + C_{\alpha,max} \quad (3)$$

where ρ_{eut} *and* ρ_α are 2650 kg/m^3 and 2700 kg/m^3, respectively, C_E *and* $C_{\alpha,max}$ are 12.6 wt% and 1.65 wt%, respectively.

The initial mushy zone is a not fully melted part of the sample, as was shown earlier. The Si concentration of the liquid phase was C_E = 12.6 wt% (concentration of the eutectic) at the bottom of the mushy zone and C_0 = 7 wt% (concentration of the alloy) at the top at the moment of the melting. The temperature difference between the *TL* and *TE* was $\Delta T = 614 - 574 = 40$ K, so the mushy zone length was $x_{mush} = \Delta T/G = 10$ mm in the case of GB1, GB2, and GB6 samples. In the case of the GB5 sample, it was only 2 mm (see Figure 3 Stage I/Part 2 in all samples) since the solidus temperature was outside of the sample. Before the solidification of the samples, one hour was waited to develop the requested thermal field. During this time, some Si diffuses from the initial mushy zone to the fully melted part, increasing the Si concentration before the initial mushy zone (temperature gradient zone melting, or TGZM [35–37]) and decreasing it in the mushy zone. Of course,

the sum average concentration of the sample's partly and whole melted part remained constant, 7% Si. The developed concentration distribution was calculated by the explicit finite difference method (EFDM). The details of this calculation can be found in [31]. The results of the calculation can be seen in Figure 12.

As the results of the Si diffusion from the initial mushy zone, in the case of samples GB1 and GB2 at the beginning of Stage I/Part 3 (this was before the initial mushy zone), the Si concentration was something higher than the initial concentration of the alloy after the resolidification. Due to the very slow sample moving velocity of S/L and E/L fronts (0.02 mm/s), the diffusion carries away some more Si from the moving mushy zone, and so, the concentration of the Part 3 decreases, and, of course, the concentration before the moving mushy zone in the melt increases. When the E/L front velocity starts to increase (Stage I/Part 4), the time for the diffusion decreases, so the concentration of Part4 increases. In Part 5, both the S/L and E/L front velocity continuously increases, the time for the diffusion decreases, and the concentration of Part 5 remains nearly constant.

In the case of Sample GB6, the process is similar, except that the velocity of the S/L and E/L front is very slow and nearly equal during the solidification. In the case of the GB5, the initial mushy zone is small, and then the concentration increases before it is negligible. This concentration increases in the first 10 mm, which isn't visible in Figure 15.

3.5. Calculation of the ΔT Temperature Range of Solidification

The temperature range of solidification depends on the actual concentration of the sample. If there is no macrosegregation, ΔT is constant throughout the sample. The Si concentration continuously varied in the four samples in our experiments, so the ΔT also concomitantly varied. Using the calculated concentrations, the ΔT can be calculated as a function of the position in the sample by the following relation:

$$\Delta T(x_s) = T_L\,(x_S) - T_E = 660 - \frac{660 - 574}{12.6}\,C(x_s) - 574 \tag{4}$$

The calculated temperature difference is also shown in Figure 13.

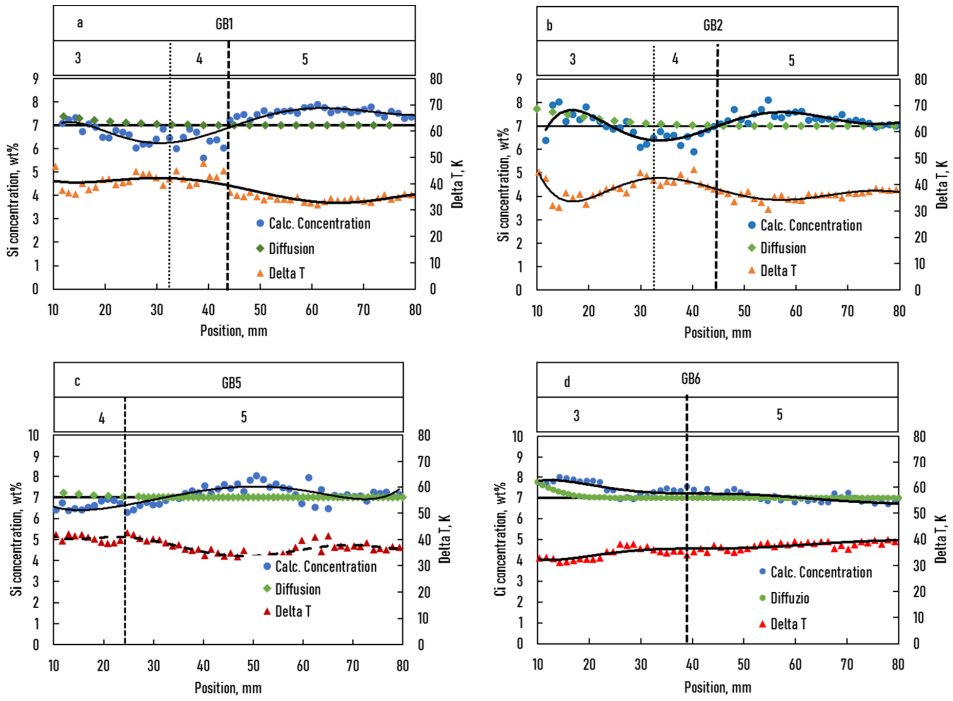

Figure 13. Calculated Si concentration from the corrected measured amount of eutectic and the calculated temperature range of solidification (*Delta T = TL − TE)* vs. position in the samples.

3.6. Secondary Dendrite Arm Spacing (SDAS, λ_2)

Most parts of the solidified solid solutions (in this case, about half of the sample) consist of secondary dendrite arms, and then the secondary dendrite arm spacing strongly affects not only the mechanical properties of the sample but the homogenization time also. The SDAS depends on the solidification parameters as follows [31]:

$$\lambda_2(x_s) = K[t_0(x_s)]^{\frac{1}{3}} = K\left(\frac{\Delta T(x_s)}{\dot{T}(x_s)}\right)^{\frac{1}{3}} = K\left(\frac{\Delta T(x_s)}{G(x_s)v(x_s)}\right)^{\frac{1}{3}} \quad (5)$$

where $\Delta T(x_s)$ is the temperature range of solidification, t_0 is the local solidification time at x_s, and K is a constant for an alloy.

As shown earlier, the temperature range of solidification depends on the actual concentration of the sample, v and G changed along with the sample, and they were different at the S/L and E/L fronts at a given x_s (Figures 3 and 4). Consequently, we used the average values of v_{av} (x_s) and G_{av} (x_s)]:

$$v_{av}(x_s) = \frac{v_{SL}(x_s) + v_{EL}(x_s)}{2} \quad (6)$$

$$G_{av}(x_s) = \frac{G_{SL}(x_s) + G_{EL}(x_s)}{2} \quad (7)$$

where $v_{SL}(x_s)$, $v_{EL}(x_s)$ and $G_{SL}(x_s)$, $G_{\text{S.L.}}(x_s)$ are the front velocities and the temperature gradients at S/L and E/L fronts, respectively. So:

$$\lambda_2(x_s) = K\left(\frac{\Delta T(x_s)}{G_{av}(x_s)v_{av}(x_s)}\right)^{\frac{1}{3}} \quad (8)$$

Compared to the measured and the calculated SDAS (Figure 14), it can be seen that they are quite similar, K = 5.2 ± 0.2, and the exponent is 1/3 in good agreement with the theory [19–25].

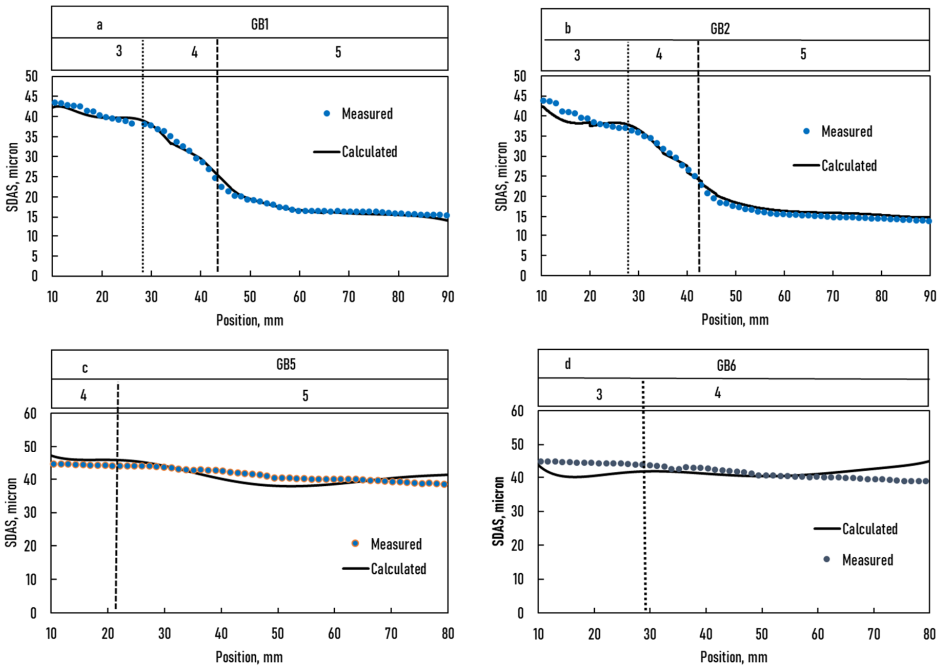

Figure 14. Measured and calculated SDAS vs. position in the sample: (**a**): GB1, (**b**): GB2, (**c**): GB5, (**d**): GB6.

The SDAS in GB1, GB2, and GB5, GB6 vs. position in the samples are practically the same, and it can be stated that the grain refinement material and the weak magnetic stirring do not affect the SDAS.

4. Discussion

4.1. Comparison of the Grain Structure of the Space and Ground-Based Experiments

4.1.1. Initial Mushy Zone

As was mentioned earlier, a significant difference between the ground-based and space samples is that before starting the solidification phase, the space samples were held at high temperatures for a long homogenization time (14,000 to 28,000 s depending on the experiment). In contrast, all GB samples were held only during 3600 s. During this period, some Si diffuses from the initial mushy zone to the fully melted part due to Temperature Gradient Zone Melting, TGZM [35–39]). This diffusion leads to an increase in the Si concentration ahead of the solid/liquid interface and a decrease in the mushy zone.

As a result of the longer holding time, more Si diffused from the mushy zone to the melted part of the sample in the case of the B2F samples than in the case of GB samples. The grain structure of the resolidified initial mushy zone of B2F samples consists of a part with only α phase (2 in Figure 15) and a part with some eutectic between the α grains (3 in Figure 15). The grain structure of the resolidified initial mushy zone of GB samples doesn't contain a part with only pure α phase (the homogenization time was short). However, the grain structure of part 2 in the B2F sample is similar to the grain structure of Section 2 of the GB samples.

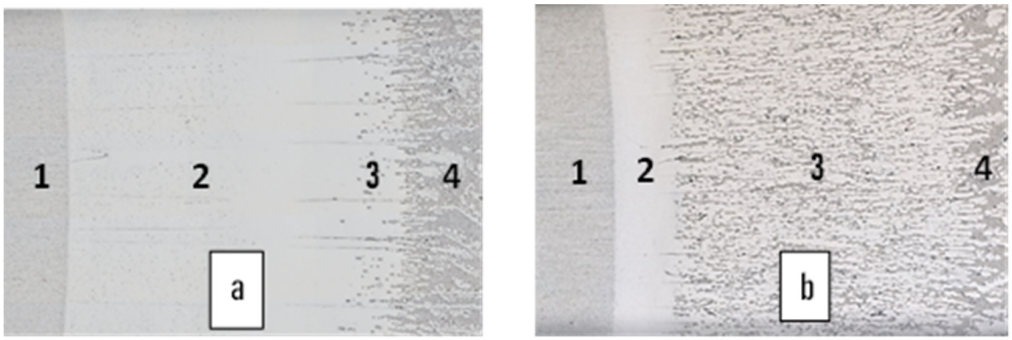

Figure 15. Microstructure of the initial mushy zone of B2F1 (**a**) and B2F5 (**b**) 1: non melted part, 2 and 3: initial mushy zone, 4: melted part.

4.1.2. Fully Melted Part

Comparision of the Grain Structure of the GB and B2F Samples

After the melting and homogenization, the GR distribution is homogeneous in the GB and B2F, B1FM5 samples [40]. As was shown in [41], the amount and the distribution of the active GR always remained similar even after several times of remelting of aluminium alloys on Earth which indicated that the sedimentation of GR could be neglected during solidification on Earth. So, the amount and the distribution GR are nearly the same in the GB and B2F samples.

As was mentioned in the introduction, the effects of the melt flow caused temperature and concentration different, can develop in the mushy zone and ahead of the S/L interface in the undercooled zone on Earth. Since the density difference between the Al and Si is small (at room temperature 2.7 g/cm^3 and 2.35 g/cm^3), the cause of the melt flow substantially is the temperature difference. Of course, in space, the melt flow is eliminated.

The new nucleus can mostly form during heterogeneous nucleation since homogenous nucleation needs more undercooling. The base of the heterogeneous nucleus would be the broken part of the dendrites or the particles of GR.

The intensity of this melt flow caused by the gravity and the stirring by 0.5 mt RMF in the mushy zone is not too strong (the permeability of the dendrite network is restricted),

and then it is not enough to break some small solid parts from the solidified dendrites. The melt flow ahead of the S/L interface in the undercooled zone is stronger than in the mushy zone. During solidifying samples containing GR, the melt flow can carry the GR to the melt part of the sample from the undercooled zone.

To take considering these facts, the developed grain structure of the B2F, B1FM5, and GB samples can explain as follows:

(i) B2F1 and B1FM5 samples (GR): there was no melt flow, and the GR distribution remained the original. With the increase of the $v_{S/L,}$ the undercooling was high enough for the heterogeneous nucleation, and the CET could be developed at a high $G_{L/S}/v_{L/S}$ (B2F1: 80 Ks/mm^2, B1FM5: 63 Ks/mm^2). The first part of the samples is columnar, and the second is elongated equiaxed.

(ii) GB1 and GM samples (GR): there was melt flow caused by gravity, the melt flow carried the GR from the undercooled zone to the melt of the sample. With the increase of the $v_{S/L,}$ the undercooling was high enough for the heterogeneous nucleation, but the CET could be developed only at a lower $G_{L/S}/v_{L/S}$ compared with the B2F1 and B1FM5 samples (GB1: 53 Ks/mm^2, B1FM5: 13 Ks/mm^2). The grain structure of the first part of the samples is columnar, and the second is elongated equiaxed.

(iii) B2F2 sample (no GR): there was melt flow caused by 0.5 mT RMF. It was not enough to break some small parts from the solidified dendrites, and the undercooling was not high enough for the homogenous nucleation, the grain structure remained columnar in the whole sample at a minimum of $G_{L/S}/v_{L/S}$ (35 Ks/mm^2).

(iv) GB2 sample (no GR): there was melt flow caused by gravity and 0.5 mT RMF. It was not enough to break some small parts from the solidified dendrites, and the undercooling was not high enough for the homogenous nucleation, the grain structure remained columnar in the whole sample at a minimum of $G_{L/S}/v_{L/S}$ (23 Ks/mm^2).

(v) B2F5 sample (GR): there was no melt flow, and the GR distribution remained the original. The $G_{S/L}$ and the $v_{S/L}$ were nearly constant in the whole sample, and the undercooling was not high enough for the homogenous nucleation, the grain structure remained columnar in the whole sample at a minimum of $G_{L/S}/v_{L/S}$ (112 Ks/mm^2).

(vi) GB5 samples (GR): there was melt flow caused by gravity, the melt flow carried the GR from the undercooled zone to the melt of the sample. The $G_{S/L}$ and the $v_{S/L}$ were nearly constant in the whole sample, and the undercooling was not high enough for the homogenous nucleation, the grain structure remained columnar in the whole sample at a minimum of $G_{L/S}/v_{L/S}$ (108).

(vii) B2F6 sample (no Gr): there was melt flow caused by 0.5 mT RMF. It was not enough to break some small parts from the solidified dendrites, and the undercooling was not high enough for the homogenous nucleation, the grain structure remained columnar in the whole sample at a minimum of $G_{L/S}/v_{L/S}$ (128 Ks/mm^2).

(viii) GB6 samples (no GR): there was melt flow caused by gravity and 0.5 mT RMF, which carried the GR from the undercooled zone to the melt of the sample. The $G_{S/L}$ and the $v_{S/L}$ were nearly constant in the whole sample, and the undercooling was not high enough for the homogenous nucleation, the grain structure remained columnar in the whole sample at a minimum of $G_{L/S}/v_{L/S}$ (88 Ks/mm^2).

Comparision of the Equiaxed Grain Structure of B2F1 and GB1 Samples

The L/W vs. position of the B2F1 and GB1 samples is shown in Figure 16a. The position in the GB1 sample is shifted by 73 mm in Figure 11 to compare the L/W of the two samples. The L/W for both samples is more than 2 but less than 4.5 except in the B2F1 sample at 148 mm, increasing to the maximum of 8. The grain structure is elongated equiaxed in both samples. The extremely high L/W in sample B2F1 can explain the issue of the shrinkage (surface pore) on the wall of the sample (Figure 16b), which can deform the dendritic network in the mushy zone and produce longer grains [30].

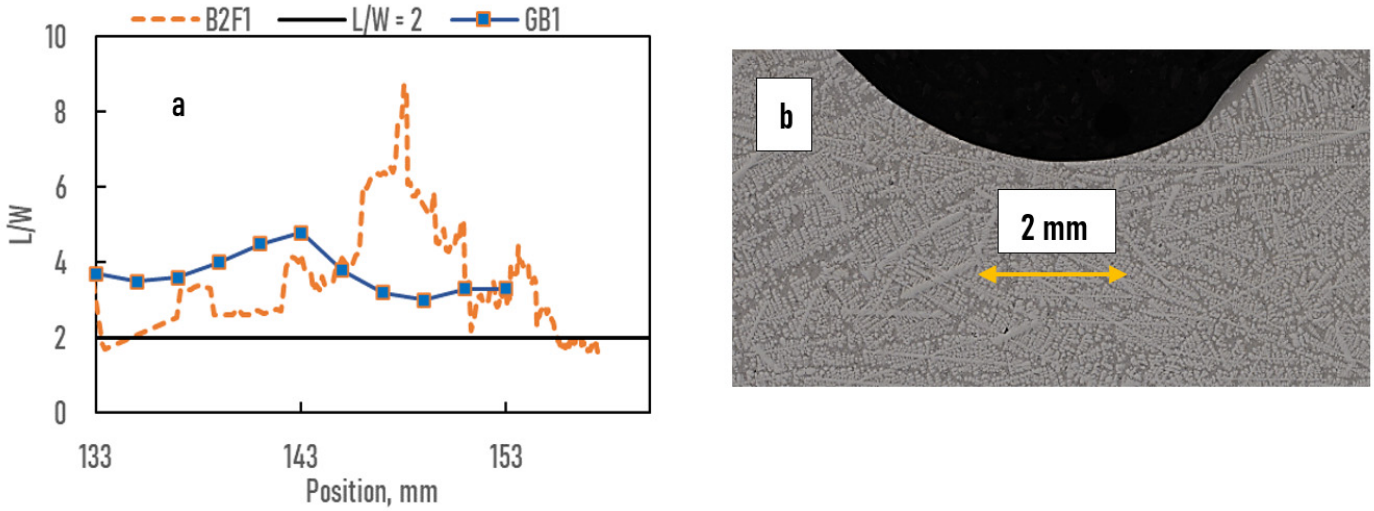

Figure 16. (**a**) L/W versus position of B2F1 and GB1 samples; (**b**) microstructure of B2F1 sample at 148 mm with a surface pore.

4.1.3. Comparing by the $v_{SL}(G_{SL})$ Function

As the G and v parameters of the GB and B2F experiments were not the same, the results of the two experiments series cannot be compared directly. Then, to compare the results of the space and the ground-based experiments, the $v_{SL}(G_{SL})$ paths were constructed, shown in Figure 13a (with grain refinement) and Figure 13b (without grain refinement).

The grain structure of the sample B2F1 from 120 to 134 mm is columnar. The CET_{min}, where elongated equiaxed grains (the elongation factor EF > 2) occurred, is at 134 mm of the sample where v_{SL} = 0.065 mm/s and G_{SL} = 5.2 K/mm, (point 3 in Figure 17b). The CET_{max} where EF is less than 2 [15] occurred at 156 mm of the sample where v_{SL}~ 3 mm/s and G_{SL} = 6.72 K/mm (it is not in the figure).

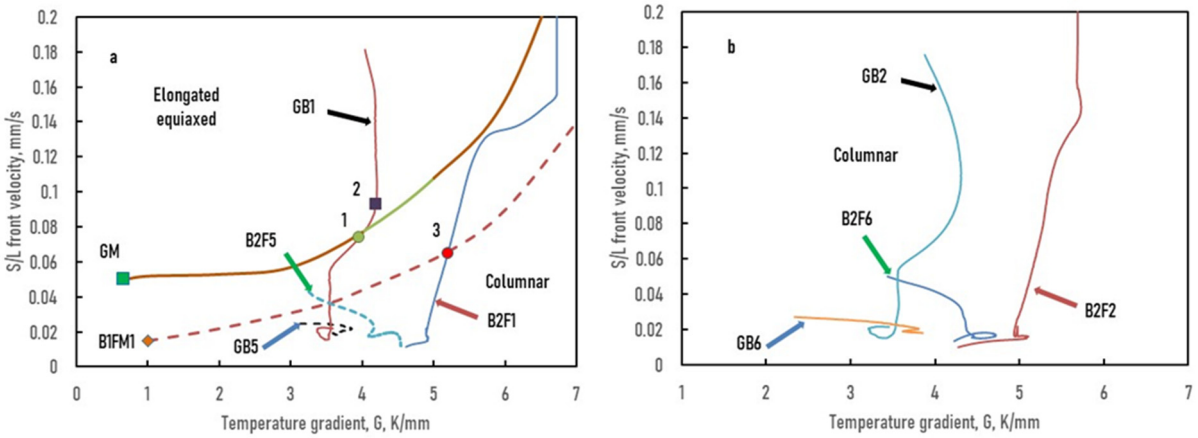

Figure 17. $v_{SL}(G_{SL})$ paths of the CETSOL Batch2 microgravity (B2F) and the ground-based (GB) experiments; (**a**) samples contain GR, (**b**) samples do not contain GR.

A space (B1FM5) and a ground-based (GM) experiment were compared in other experiment series [29]. The alloy was the same and contained GR. The B1FM5 and GM samples were elaborated using the Low Gradient Furnace (LGF) on the ISS. The temperature gradient (G_{SL}) and the solid/liquid front velocity (v_{SL}) versus the position in the samples were practically the same. The CET_{min} occurred at G_{SL} = 0.65 K/mm, v_{SL} = 0.05 mm/s and G_{SL} = 0.95 K/mm, v_{SL} = 0.015 mm/s in the case of GM and B1FM5 samples, respectively.

Based on these results, two different hypothetical CET_{min} curves were constructed for the space and the ground-based experiments (Figure 17a). These are considered hy-

pothetical since these curves were constructed based on only two measured points and the known form of this curve in literature [15]. The solid and dashed lines represent the CET_{min} for the ground and the space experiment, respectively. From these two curves, at a given temperature gradient, the CET_{min} will occur at a higher solid/liquid front velocity on the ground than in space. For example, at the point 1 (G_{SL} = 3.9 K/mm), v_{SL} = 0.074 mm/s and 0.044 mm/s, and at point 3 (G_{SL} = 5.2 K/mm) v_{SL} = 0.12 mm/s and 0.065 mm/s in the cases on the ground and in the space, respectively. Similarly, at a given S/L front velocity, the CET_{min} will occur at a smaller temperature gradient. For example, at point 3 (v_{SL} = 0.065 mm/s) G_{SL} = 5.2 K/mm and 3.4 K/mm in the cases on the ground and the space, respectively. The cause of this difference would be the buoyancy flow, which changes the concentration difference just ahead of the dendrite tip and bring some small broken solid particle from the mushy zone to melt ahead of the S/L front.

The $v_{SL}(G_{SL})$ paths are shown in Figure 13b in the case of the B2F2, B2F5, and B2F6 space samples and the GB2, GB5, and GB6 ground-based samples do not contain G.R. The grain structure was columnar for all samples in the investigated G_{SL} and v_{SL} range. Figure 13 $v_{SL}(G_{SL})$ paths of the CETSOL Batch2 microgravity (B2F) and the ground based (GB) experiments; a: samples contain GR, b: samples does not contain GR.

4.2. Comparison of the Initial Concentration Distribution and the Amount of Eutectic of the Space and Ground-Based Solidified Samples

The cause of the difference in the concentration distribution was the different "homogenization time". As mentioned earlier, in the case of the space experiments, it was longer, 28,000 s and 14,000 s for B2F1, B2F2, and B2F5, B2F6 respectively, while in the case of the ground-based experiments, it was only 3600 s. As a result, more Si diffuses to the melt from the initial mushy zone in the case of the space samples, so the initial concentration of B2F samples was higher than the GB samples.

The eutectic was formed between the secondary dendrite arms as a degenerated eutectic (the α solid solution part of the eutectic solidified on the α solid solution dendrites) and between the coarse columnar primary arms as large eutectic pockets both in the B2F and GB samples. The amount of eutectic in the B2F samples is something higher than in the GB samples in Part 3, due to the higher Si concentration.

4.3. Comparison of the SDAS of the Space and Ground-Based Experiments

The dendrite arm spacing (DAS) was determined using the linear intercept method in the case of B2F samples [26] in contrast to the GB samples, where the true SDAS was measured by another method described in Section 2.5.2. It must be mentioned that the DAS measured by the intercept method is not equal to the true SDAS and is often slightly higher due to the measurement method.

For both the B2F and GB samples, the DAS could be calculated with the diffusion type coarsening equation, where the kinetic constant is 1/3. It means that the magnetic stirring by 0.5 mT (B2F2, B2F6 samples), the gravity effect alone (GB1, GB5 samples), and the gravity effect overlapped with the magnetic stirring (GB2, GB6 samples) can not affect the coarsening of the SDAS.

The agreement between the measured DAS and the SDAS calculated by Equation (8) was suitable for all B2F samples even though the DAS generally overestimates the SDAS, as discussed above. For B2F1 and B2F2 samples, K was 7.5, and for B2F5 and B2F6 samples, 10 and 9, respectively. The K was 5.2 for all GB samples, meaning that the DAS was 1.44 times more than the SDAS for B2F1 and B2F2 samples, and 1.73 and 1.92 times more for B2F5 and B2F6 samples, respectively, at the same G_{av} and v_{av}. The different K values can be explained by the measurement method of DAS.

5. Summary and Conclusions

During ground-based solidification, buoyancy flow can develop by the density difference in the hypoeutectic type of the alloys, such as the Al-7 wt% Si alloy. The buoyancy flow

can affect the thermal field, solute distribution in the melt, and the position and amount of the new grains. As solidification is a very complex process, it isn't very easy to separate the different effects. Under microgravity conditions, natural convection does not exist or is strongly damped due to the absence of buoyancy force. Therefore, experiments in microgravity conditions provide unique benchmark data for pure diffusive solidification conditions. Compared to the results of the ground-based and microgravity experiments, it is possible to get information on the effect of gravity (buoyancy force).

In some earlier papers, the results of four microgravity solidification experiments were shown [26–31]. These experiments were performed on grain refined and non-grain refined Al-7 wt% Si alloy onboard the International Space Station (ISS) in the Materials Science Lab (MSL) in the framework of the CETSOL project. In this work, four "mirror" experiments were implemented on the ground with the same alloys and similar solidification parameters (sample moving velocity, temperature gradient, magnetic stirring) to examine the effect of the gravity-induced buoyancy flow (GB samples). The grain structure (especially the Columnar /Equiaxed Transition, CET) and the secondary dendrite arm spacing (SDAS) were investigated. Based on the comparison of the results of ground-based and space experiments can be stated as follows:

(i) As a result of the longer holding time, more Si diffused from the mushy zone to the melted part of the sample in the case of the B2F samples than in the case of GB samples. The grain structure of the resolidified initial mushy zone of B2F samples consists of a part without eutectic. It is only the α phase with cellular structure and a part with some eutectic between the α grains. The grain structure of the resolidified initial mushy zone of GB samples does not contain only the α phase (the homogenization time was short).

(ii) Without grain refinement, due to homogeneous nucleation did not form any new nucleus before the growing columnar dendrites, the grain structure of the samples remained columnar at the used temperature gradient and S/L front velocity range both in the B2F and GB sample.

(ii) With grain refinement, due to heterogeneous nucleation forming some new nucleus before the growing columnar dendrites, the grain structure of the samples changed from columnar to elongated equiaxed but only at a relatively high S/L front velocity both in the B2F and GB samples. The necessary $G_{S/L}/v_{S/L}$ is higher in the case of the ground-based experiment than in the space experiment.

(iii) The melt flow caused by the gravity and 0.5 mT RMF could not change the grain structure

(iv) Based on the results of the B1FM5, B2F1, GM and GB1 samples, two different hypothetical, new CET_{min} lines were constructed for the space and the ground-based experiments. From these two lines it can be stated that at a given temperature gradient, the CET_{min} will occur at a higher solid/liquid front velocity on the ground as in space. Similarly, at a given S/L front velocity, the CET_{min} will occur at a smaller temperature gradient.

(v) The secondary dendrite arm spacing (SDAS, λ_2) is calculatable from the average temperature gradient (G_{av}) and front velocity (v_{av}) with the well-known equation:

$$\lambda_2(x_s) = K\left(\frac{\Delta T(x_s)}{G_{av}(x_s)v_{av}(x_s)}\right)^{\frac{1}{3}}$$

considering the $\Delta T = TL - TE$. temperature range of solidification.

The 1/3 kinetic constant means that the coarsening process of secondary dendrite arms was diffusion type, the effect of the gravity and the 0.5 mT magnetic stirring could not change the type of the process. The K was 5.2 for all G.B. samples, meaning that the DAS was 1.44 times more than the SDAS for B2F1 and B2F2 samples, and 1.73 and 1.92 times more for B2F5 and B2F6 samples, respectively, at the same G_{av} and v_{av}. The different K values can be explained by the different measurement methods of SDAS and DAS. The SDAS was measured perpendicular to the secondary dendrite arms, while DAS by the intercept method overestimates the actual SDAS. The SDAS vs. local solidification time,

calculated from the *DeltaT*, *G*, and *v* was usable in the case of GB and the B2F samples, too, with a 1/3 exponent. Only the constant was different, which came from the different measuring methods. So, the secondary dendrite arm coarsening process is identical in space and on the ground.

Author Contributions: Conceptualization, A.R. (András Roósz); funding acquisition, A.R. (András Roósz) and G.Z.; investigation, Y.L., N.M.-N., G.Z., M.S., A.R. (Arnold Rónaföldi) and Z.V.; methodology, A.R. (András Roósz); project administration, A.R. (András Roósz) and G.Z.; software, A.R. (Arnold Rónaföldi); supervision, A.R. (András Roósz), G.Z., Z.V. and H.N.-T.; validation, A.R. (András Roósz), A.R. (Arnold Rónaföldi), Y.L., N.M.-N., G.Z., H.N.-T., M.S. and Z.V.; writing—original draft, A.R. (András Roósz) and Z.V.; writing—review and editing, A.R. (András Roósz), N.M.-N., H.N.-T. and Z.V. All authors have read and agreed to the published version of the manuscript.

Funding: This research was funded by the European Space Agency under the CETSOL (columnar-to-equiaxed solidification processes), ESA MAP (AO-99-117) and the CETSOL/HUNGARY ESA PRODEX (No 4000131880/NL/SH) projects, the FWF-NKFIN (130946 ANN) joint project, the French National Space Agency (CNES), and the German BMWi/DLR under FKZ 50WM1743 and FKZ 50WM2043.

Data Availability Statement: Data may be requested from the corresponding authors.

Conflicts of Interest: The authors declare no conflict of interest.

References

1. Gomes, C.H.U.; Kikuchi, R.H.L.; Barros, A.D.S.; Da Silva, J.N.S.; Silva, M.A.P.D.S.D.; Moreira, A.L.S.; Da Rocha, O.F.L. On the Natural Convection in the Columnar to Equiaxed Transition in Directionally Solidified Aluminum-based Binary and Multicomponent Alloys. *Mater. Res.* **2015**, *18*, 1362–1371. [CrossRef]
2. Reinhart, G.; Gandin, C.A.; Mangelinck-Noël, N.; Nguyen-Thi, H.; Spinelli, J.E.; Baruchel, J.; Billia, B. Influence of natural convection during upward directional solidification: A comparison between in situ X-ray radiography and direct simulation of the grain structure. *Acta Mater.* **2013**, *61*, 4765–4777. [CrossRef]
3. Dupouy, M.; Camel, D. Effects of gravity on columnar dendritic growth of metallic alloys: Flow pattern and mass transfer. *J. Cryst. Growth* **1998**, *183*, 469–489. [CrossRef]
4. Rerko, R.S.; de Groh, H.C.; Beckermann, C. Effect of melt convection and solid transport on macrosegregation and grain structure in equiaxed Al–Cu alloys. *Mater. Sci. Eng. A* **2003**, *347*, 186–197. [CrossRef]
5. Nguyen-Thi, H.; Reinhart, G.; Billia, B. On the interest of microgravity experimentation for studying convective effects during the directional solidification of metal alloys. *Comptes Rendus Mécanique* **2017**, *345*, 66–77. [CrossRef]
6. Spinelli, J.E.; Ferreira, I.L.; Garcia, A. Influence of melt convection on the columnar to equiaxed transition and microstructure of downward unsteady-state directionally solidified Sn-Pb alloys. *J. Alloy. Compd.* **2004**, *384*, 217–226. [CrossRef]
7. Shevchenko, N.; Neumann-Heyme, H.; Pickmann, C.; Schaberger-Zimmermann, E.; Zimmermann, G.; Eckert, K.; Eckert, S. Investigations of fluid flow effects on dendritic solidification: Consequences on fragmentation, macrosegregation and the influence of electromagnetic stirring. *IOP Conf. Series: Mater. Sci. Eng.* **2017**, *228*, 012005. [CrossRef]
8. Flemings, M.C. Our Understanding of Macrosegregation. Past and Present. *ISIJ Int.* **2000**, *40*, 833–841. [CrossRef]
9. Beckermann, C. Modelling of macrosegregation: Applications and future needs. *Int. Mater. Rev.* **2002**, *47*, 243–261. [CrossRef]
10. Guillemot, G.; Gandin, C.-A.; Combeau, H. Modeling of Macrosegregation and Solidification Grain Structures with a Coupled Cellular Automaton-Finite Element Model. *ISIJ Int.* **2006**, *46*, 880–895. [CrossRef]
11. Griffiths, W.; Xiao, L.; McCartney, D. The influence of bulk liquid natural convection on the formation of the equiaxed regions in Al □Cu and Al □Si alloys. *Mater. Sci. Eng. A* **1996**, *205*, 31–39. [CrossRef]
12. Zimmermann, G.; Pickmann, C.; Hamacher, M.; Schaberger-Zimmermann, E.; Neumann-Heyme, H.; Eckert, K.; Eckert, S. Fragmentation-driven grain refinement in directional solidification of AlCu10wt-% alloy at low pulling speeds. *Acta Mater.* **2017**, *126*, 236–250. [CrossRef]
13. Ruvalcaba, D.; Mathiesen, R.; Eskin, D.; Arnberg, L.; Katgerman, L. In situ observations of dendritic fragmentation due to local solute-enrichment during directional solidification of an aluminum alloy. *Acta Mater.* **2007**, *55*, 4287–4292. [CrossRef]
14. Burden, M.; Hebditch, D.; Hunt, J. Macroscopic stability of a planar, cellular or dendritic interface during directional freezing. *J. Cryst. Growth* **1973**, *20*, 121–124. [CrossRef]
15. Hunt, J. Steady state columnar and equiaxed growth of dendrites and eutectic. *Mater. Sci. Eng.* **1984**, *65*, 75–83. [CrossRef]
16. Bedel, M.; Tveito, K.; Založnik, M.; Combeau, H.; M'Hamdi, M. A model study of the impact of the transport of inoculant particles on microstructure formation during solidification. *Comput. Mater. Sci.* **2015**, *102*, 95–109. [CrossRef]
17. Tveito, K.O.; Bedel, M.; Založnik, M.; Combeau, H.; M'Hamdi, M.; Kumar, A.; Dutta, P. Numerical study of the impact of inoculant and grain transport on macrosegregation and microstructure formation during solidification of an Al-22%Cu alloy. *IOP Conf. Ser. Mater. Sci. Eng.* **2012**, *33*, 012089. [CrossRef]

18. Heyvaert, L.; Bedel, M.; Založnik, M.; Combeau, H. Modeling of the Coupling of Microstructure and Macrosegregation in a Direct Chill Cast Al-Cu Billet. *Met. Mater. Trans. A* **2017**, *48*, 4713–4734. [CrossRef]
19. Kirkwood, D. A simple model for dendrite arm coarsening during solidification. *Mater. Sci. Eng.* **1985**, *73*, L1–L4. [CrossRef]
20. Flemings, M.C. Coarsening in Solidification Processing. *Mater. Trans.* **2005**, *46*, 895–900. [CrossRef]
21. Kurz, W.; Fisher, D.J. *Fundamentals of Solidification*, 4th ed.; Trans Tech Publications Ltd.: Zurich, Switzerland, 1998.
22. Kurz, W.; Fisher, D. Dendrite growth at the limit of stability: Tip radius and spacing. *Acta Met.* **1981**, *29*, 11–20. [CrossRef]
23. Furer, U.; Wunderlin, R. *Metal Solidification*; DGM Fachber: Stuttgart, Germany, 1977; Volume 144.
24. Roósz, A. The Effect of Temperature Gradient and Primary Arm Tip Velocity on Secondary Dendrite Arm Spacing at Steady-state Conditions Solidification. *Cast Met.* **1988**, *1*, 223–226. [CrossRef]
25. Steinbach, S.; Ratke, L. The influence of fluid flow on the microstaructure of directionally solidified AlSi base alloys. *Metall. Mater. Trans. A* **2007**, *38*, 1388–1394. [CrossRef]
26. Li, Y.; Mangelinck-Noël, N.; Zimmermann, G.; Sturz, L.; Nguyen-Thi, H. Modification of the microstructure by rotating magnetic field during the solidification of Al-7 wt.% Si alloy under microgravity. *J. Alloy. Compd.* **2020**, *836*, 155458. [CrossRef]
27. Li, Y.; Mangelinck-Noël, N.; Zimmermann, G.; Sturz, L.; Nguyen-Thi, H. Comparative study of directional solidification of Al-7 wt% Si alloys in Space and on Earth: Effects of gravity on dendrite growth and Columnar-to-equiaxed transition. *J. Cryst. Growth* **2019**, *513*, 20–29. [CrossRef]
28. Liu, D.; Mangelinck-Noël, N.; Gandin, C.-A.; Zimmermann, G.; Sturz, L.; Thi, H.N.; Billia, B. Structures in directionally solidified Al–7wt.% Si alloys: Benchmark experiments under microgravity. *Acta Mater.* **2014**, *64*, 253–265. [CrossRef]
29. Li, Y.Z.; Mangelinck-Noël, N.; Nguyen-Thi, H.; Zimmermann, G.; Sturz, L.; Cool, T.; Gulsoy, E.B.; Voorhees, P.W. Critical parameters concerning the columnar-to-equiaxed transition in solidification processing. In Proceedings of the 6th Decennial International Conference on Solidification Processing, Old Windsor, UK, 25–28 July 2017; pp. 317–321.
30. Li, Y.; Mangelinck-Noël, N.; Zimmermann, G.; Sturz, L.; Nguyen-Thi, H. Effect of solidification conditions and surface pores on the microstructure and columnar-to-equiaxed transition in solidification under microgravity. *J. Alloy. Compd.* **2018**, *749*, 344–354. [CrossRef]
31. Roósz, A.; Rónaföldi, A.; Li, Y.; Mangelinck-Noël, N.; Zimmermann, G.; Nguyen-Thi, H.; Svéda, M.; Veres, Z. Influence of Solidification Parameters on the Amount of Eutectic and Secondary Arm Spacing of Al–7wt% Si Alloy Solidified under Microgravity. *Crystals* **2022**, *12*, 414. [CrossRef]
32. Zimmermann, G.; Sturz, L.; Yuze, L.; Nguyen-Thi, H.; Mangelinck-Noël, N.; Fleurisson, R.; Guillemot, G.; Gandin, C.-A.; Mcfadden, S.; Mooney, R.P.; et al. Columnar and equiaxed solidification within in the framework of the ESA MAP project CETSOL. In Proceedings of the Seventh International Conference on Solidification and Gravity, Miskolc-Lillafüred, Hungary, 3–6 September 2018; pp. 17–26.
33. Veres, Z.; Roósz, A.; Rónaföldi, A.; Sycheva, A.; Svéda, M. The effect of melt flow induced by RMF on the meso- and micro-structure of unidirectionally solidified Al–7wt.% Si alloy Benchmark experiment under magnetic stirring. *J. Mater. Sci. Technol.* **2021**, *103*, 197–208. [CrossRef]
34. Kasperovich, G.; Volkmann, T.; Ratke, L.; Herlach, D. Microsegregation during Solidification of an Al-Cu Binary Alloy at Largely Different Cooling Rates (0.01 to 20,000 K/s): Modeling and Experimental Study. *Met. Mater. Trans. A* **2008**, *39*, 1183–1191. [CrossRef]
35. Dantzig, J.A.; Rappaz, M. *Solidification: Revised & Expanded*; EPFL Press: New York, NY, USA, 2016.
36. Phillion, A.; Založnik, M.; Spindler, I.; Pinter, N.; Aledo, C.-A.; Salloum-Abou-Jaoude, G.; Thi, H.N.; Reinhart, G.; Boussinot, G.; Apel, M.; et al. Evolution of a mushy zone in a static temperature gradient using a volume average approach. *Acta Mater.* **2017**, *141*, 206–216. [CrossRef]
37. Thi, H.N.; Drevet, B.; Debierre, J.; Camel, D.; Dabo, Y.; Billia, B. Preparation of the initial solid–liquid interface and melt in directional solidification. *J. Cryst. Growth* **2003**, *253*, 539–548. [CrossRef]
38. Thi, H.N.; Reinhart, G.; Buffet, A.; Schenk, T.; Mangelinck-Noël, N.; Jung, H.; Bergeon, N.; Billia, B.; Härtwig, J.; Baruchel, J. In situ and real-time analysis of TGZM phenomena by synchrotron X-ray radiography. *J. Cryst. Growth* **2008**, *310*, 2906–2914. [CrossRef]
39. Bergeon, N.; Reinhart, G.; Mota, F.L.; Mangelinck-Noël, N.; Nguyen-Thi, H. Analysis of gravity effects during binary alloy directional solidification by comparison of microgravity and Earth experiments with in situ observation. *Eur. Phys. J. E* **2021**, *44*, 98. [CrossRef]
40. Karagadde, S.; Yuan, L.; Shevchenko, N.; Eckert, S.; Lee, P. 3-D microstructural model of freckle formation validated using in situ experiments. *Acta Mater.* **2014**, *79*, 168–180. [CrossRef]
41. Murphy, A.; Mathiesen, R.; Houltz, Y.; Li, J.; Lockowandt, C.; Henriksson, K.; Zimmermann, G.; Melville, N.; Browne, D. XRMON-SOL: Isothermal equiaxed solidification of a grain refined Al–20wt%Cu alloy. *J. Cryst. Growth* **2016**, *440*, 38–46. [CrossRef]